

# Fast spectral line calculations with the escape probability method and tests with synthetic observations of interstellar clouds

Mika Juvela

Department of Physics, P.O.Box 64, FI-00014, University of Helsinki, Finland, [mika.juvela@helsinki.fi](mailto:mika.juvela@helsinki.fi)

Received September 15, 1996; accepted March 16, 1997

## ABSTRACT

*Context.* Radiative transfer effects need to be taken into account when analysing spectral line observations. When the data are not sufficient for detailed modelling, simpler methods are needed. The escape probability formalism (EPF) is one such tool.

*Aims.* We wish to quantify the model errors in the EPF analysis of interstellar clouds and cores.

*Methods.* We introduce PEP, a parallel program for calculating fast EPF parameters quickly. We model full radiative transfer to generate synthetic observations for various cloud models. These are examined with the PEP program, and their results are compared to the actual beam-averaged kinetic temperatures, column densities, and volume densities.

*Results.* PEP enables the calculations of even millions of parameter combinations in a matter of seconds. However, the simple assumptions of EPF can lead to significant errors. In the tests the errors were typically within a factor of two, but could in some cases reach an order of magnitude. The model errors are thus similar or even larger than the statistical errors caused by the typical observational noise. Due to degeneracies, parameter combinations are better constrained than the individual parameters. The model errors could be reduced by using full radiative transfer modelling. However, in the absence of full knowledge of the source structure, the errors are difficult to quantify. We also present a method for approximate handling of hyperfine structure lines in EPF calculations.

*Conclusions.* Both the observational statistical errors and the model errors need to be considered when estimating the reliability of EPF results. Full radiative transfer modelling is needed to better understand the true uncertainties.

**Key words.** ISM: molecules – techniques: spectroscopic – radiative transfer – line: formation – ISM: clouds – methods: numerical

## 1. Introduction

Radiative transfer (RT) is central to many astrophysics problems from the analysis of observations to the modelling of the thermal balance, ionisation and chemistry of interstellar clouds. The present paper concentrates on a more limited problem, the role of radiative transfer in the direct analysis of spectral line observations. RT modelling can take into account the assumed three-dimensional distributions of density, velocity, and kinetic temperature, the fractional abundances of the examined species, as well as other sources of radiation and opacity. However, RT is typically treated using some simplifications (Neufeld & Kaufman 1993; Neufeld et al. 1995; Juvela et al. 2003; Peters et al. 2011; Juvela & Ysard 2011; Commerçon et al. 2010; Tomida et al. 2013).

There are many publicly available RT programs, enabling one to estimate source properties by fitting a source model against the shapes and intensities of the observed lines (e.g. Bernes 1979; Juvela 1997; Harries et al. 2019; Hogerheijde & van der Tak 2000; Dullemond & Turolla 2000; van Zadelhoff et al. 2002; Juvela 2020). However, observations are often insufficient to constrain complex models, and one may prefer faster methods with inherently fewer free parameters. The local thermodynamic equilibrium (LTE) is the simplest option, providing an analytical mapping between the source parameters and the line intensities. The LTE assumption is sometimes justified, when the level populations can be expected to be close to the LTE values due to high density or high optical depths. However, all sources show some deviations from the LTE. For example, due to the decreasing density and increasing probability for

the emitted photons to escape, the excitation tends to be lower in the surface layers of molecular clouds. Deviations from LTE become more obvious with better measurements, as the excitation temperatures  $T_{\text{ex}}$  can vary both spatially and between transitions. Therefore, there is need for methods that are easier and faster than the full radiative transfer modelling but still able to capture the main effects of the non-LTE excitation.

The escape probability formalism (EPF) is one such method (Sobolev 1960; de Jong et al. 1975; Goldreich & Scoville 1976). The source is described by its kinetic temperature  $T_{\text{kin}}$ , column density per velocity interval  $dN/dv$ , and volume density  $n$ . The same values are assumed to apply to the whole source. EPF uses the parameter  $\beta$  to describe the photon escape probability, what fraction of the emitted photons leaves the source without being reabsorbed. With assumptions of the source geometry, the parameter  $\beta$  and the local radiation field can be estimated self-consistently with the level populations, thus allowing deviations from the LTE. The escape probability  $\beta$  is effectively the same for the whole source but can vary between transitions.

In this paper we present PEP, a new parallel program for EPF analysis of spectral lines. The program can also be run on graphics processing units (GPUs), with thus potential further speed-up for studies of very large parameter spaces ( $T_{\text{kin}}$ ,  $dN/dv$ ,  $n$ ). We use the program to analyse far-infrared and radio spectral lines for a series of interstellar cloud models. These include spherical clouds and more realistic clumps extracted from a 3D magnetohydrodynamic (MHD) simulation. Sources have strong density variations, and the MHD models further spatial variations of velocity, kinetic temperature, and optionally of fractional abundances. We use 3D non-LTE radiative transfer modelling to cal-

culate spectra for several molecules, analyse these synthetic observations with the PEP program, and compare results to reference values extracted from the cloud models. The synthetic observations are used without added noise or calibration errors. Our study thus concentrates on the role of the model errors that result from simplifying the complex 3D objects into a single set of scalar  $T_{\text{kin}}$ ,  $n$ , and  $dN/dv$  values. This is complementary to previous studies that have examined the errors resulting from observational noise. Those errors can be estimated locally around the  $\chi^2$  minimum or preferably analysing the full  $\chi^2$  space with direct Monte Carlo (e.g. Bron et al. 2018) or Markov chain Monte Carlo (MCMC) methods or with parameter grids fully covering the relevant 3D parameter space (e.g. Tunnard et al. 2015; Tunnard & Greve 2016; Roueff et al. 2024).

The paper is organised as follows. The EPF methods and the PEP program are described in Sect. 2. In Sect. 3, the PEP results are compared against calculations performed with the RADEX program (van der Tak et al. 2007) to confirm their accuracy. To quantify the typical model errors in EPF analysis, we examine in Sect. 4.1 a series of spherically symmetric cloud models and then in Sect. 4.2 more realistic observations of inhomogeneous clumps extracted from a 3D MHD cloud simulations. We discuss the findings in Sect. 5 before listing the main conclusions in Sect. 6. One potential way of handling hyperfine structure (HFS) lines in EPF calculations is discussed further in Appendix A.

## 2. Methods

In EPF the radiation field intensity is a weighted average of the local emission the external background  $I_{\text{bg}}$ ,

$$J_\nu = [1 - \beta]\Lambda(S_\nu) + \beta I_{\text{bg},\nu}. \quad (1)$$

Here  $\beta$  is the photon escape probability. The local emission is written with the  $\Lambda$  operator that formally operates on the source function  $S_\nu$  (the ratio of emission and absorption coefficients), the result being that part of  $J$  that is caused by emission from the medium.. The intensity  $J_\nu$  is used to solve level populations  $n_i$  from the statistical equilibrium equations, each level  $i$  having an equation

$$n_i \sum_j [A_{ij} + B_{ij}J_{ij} + C_{ij}(T_{\text{kin}})n'] = \sum_j n_j [A_{ji} + B_{ji}J_{ij} + C_{ji}(T_{\text{kin}})n'], \quad (2)$$

Here  $A$  are the Einstein coefficients for spontaneous emission,  $B$  the coefficients for stimulated transitions,  $C$  the collisional coefficients ( $[\text{cm}^3 \text{s}^{-1}]$ ),  $n'$  the density of the colliding particles, and  $J_{ij}$  the radiation field intensity at the frequency of the transition  $i \rightarrow j$ . The equation is written for arbitrary levels  $i$  and  $j$ , but spontaneous transitions are possible only to a lower energy level ( $A_{ij} = 0$  for  $j \geq i$ ) and radiative transitions (non-zero terms  $A_{ij}$  and  $B_{ij}$ ) are further limited by selection rules. The density  $n'$  and the kinetic temperature  $T_{\text{kin}}$  enter the problem via the coefficients  $C$ .

The radiation field and the level populations are coupled via the photon escape probability  $\beta$ , which depends on the optical depth of the transition

$$\tau_{ul} = \frac{h\nu}{4\pi} [N_l B_{lu} - N_u B_{ul}] \phi(\nu). \quad (3)$$

Indices  $l$  and  $u$  refer explicitly to the lower and upper energy levels of the transition.  $N_l$  and  $N_u$  are the corresponding column densities that, in the case of a homogeneous medium, are directly

the product of the volume density and the linear source size  $s$  (e.g.  $N_l = n_l s$ ). The level population ratios follow the Boltzmann equation

$$\frac{n_i}{n_j} = \frac{g_i}{g_j} e^{-(E_i - E_j)/(kT)}, \quad (4)$$

where  $g$  are the statistical weights,  $E$  the level energies, and  $k$  the Boltzmann constant. In the case of LTE,  $T$  would be equal to the kinetic temperature. More generally, the equation defines an excitation temperature  $T_{\text{ex}}$  that corresponds to the actual level populations.

EPF gives self-consistent values for the optical depths, the escape probabilities  $\beta$ , and the excitation that can now deviate from LTE. For  $\beta < 1$  the excitation is no longer determined by collisions only, typically resulting in  $T_{\text{ex}} < T_{\text{kin}}$ . However, EPF assumes a single value of density and kinetic temperature and a single set of level populations for the entire source. The values of  $\beta$  are based on assumptions of the source size and geometry or, in the case of the large velocity gradient (LVG) models, a velocity field that defines a finite source region that can interact via radiation. PEP<sup>1</sup> uses the same three alternatives included in RADEX. These correspond to a slab geometry, a homogeneous sphere, and an LVG model (sphere with constant radial velocity gradient). These result in different expressions for  $\beta$  as the function of optical depth van der Tak et al. (see 2007).

PEP calculations start with LTE level populations at the temperature of  $T_{\text{kin}}$ . Together with the other inputs,  $n$  and  $dN/dv$ , this provides values of optical depth and  $\beta$  for each transition. Instead of explicitly calculating emission via  $\Lambda(S)$ , the statistical equilibrium equations are modified by scaling the Einstein coefficients with  $\beta$ . This is the more robust alternative and analogous to the idea of accelerated lambda iterations (Cannon 1973; Rybicki & Hummer 1992). When the level populations are updated, the values of  $\tau$  and  $\beta$  also change, resulting in new estimates for  $J_\nu$ . The calculations be must iterated until the level populations have converged to their final values. The convergence criterion in PEP is based on the relative changes of the level populations during one iteration. Because convergence slows down at high optical depths, some care is needed in using tolerances that are appropriate for the examined model.

## 3. Testing of the PEP program

We compared the PEP results to those calculated with the RADEX program (van der Tak et al. 2007). Tests were performed using CO, CS and HCO<sup>+</sup> and their isotopomers, as well as the rotational spectrum of p-H<sub>2</sub>O. The molecular data were taken from the LAMDA database (Schöier et al. 2005).

Figure 1 shows examples of results for the first seven transitions of CO, HCO<sup>+</sup>, and p-H<sub>2</sub>O, the first transitions here meaning the transitions between the lowest  $J$  levels. The models cover a range of optical depths from optically thin to optically very thick. The relative populations of the  $J = 7$  level are  $\sim 10^{-7}$ , and after  $J = 7 - 6$  the transitions have  $T_{\text{R}} < 1 \mu\text{K}$ , values far below the detection threshold of typical observations. The match between the PEP and RADEX results is good, both in this case using  $\beta$  values for the LVG case.

For calculations a single set of parameters RADEX is faster, but PEP is more efficient when results are needed for tens of parameter combinations. The difference becomes significant for large parameter grids, potentially more so if calculations can

<sup>1</sup> [http://www.interstellarmedium.org/radiative\\_transfer/pep/](http://www.interstellarmedium.org/radiative_transfer/pep/)

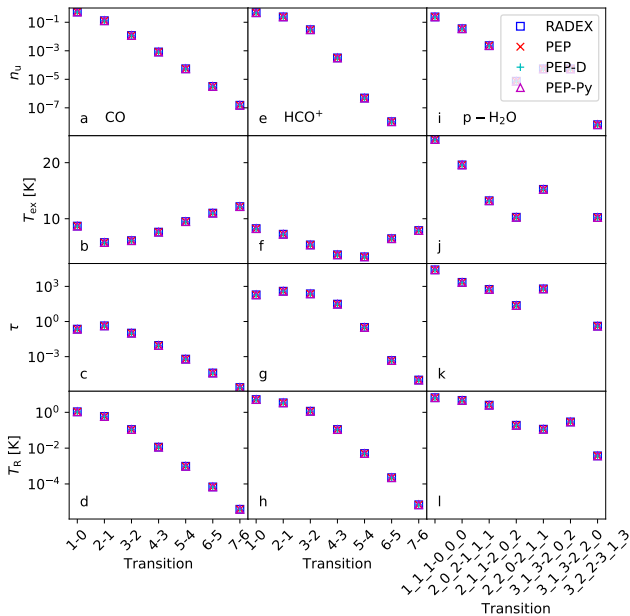


**Fig. 1.** PEP and RADEX results for density  $n(\text{H}_2) = 10^3 \text{ cm}^{-3}$ , column density of the species  $N = 10^{15} \text{ cm}^{-2}$ , and a  $1 \text{ km s}^{-1}$  linewidth. The temperature is  $T_{\text{kin}} = 20 \text{ K}$  for the CO (left frames),  $T_{\text{kin}} = 10 \text{ K}$  for the  $\text{HCO}^+$  (middle frames), and  $T_{\text{kin}} = 100 \text{ K}$  for the  $\text{H}_2\text{O}$  (right frames) runs. The plots show the fractional upper level population  $n_u$ , excitation temperature  $T_{\text{ex}}$ , optical depth  $\tau$ , and the radiation temperature  $T_{\text{R}}$  for the first seven transitions. PEP results are shown for single-precision (PEP) and double-precision (PEP-D) runs and for a pure Python implementation without parallelisation (“PEP-Py”).

be done on a GPU with single-precision floating point arithmetic (Appendix B). Figure 1 also shows results for a non-parallel, double-precision Python version. Figure 2 shows the populations for the 22 lowest energy levels in a  $T_{\text{kin}} = 70 \text{ K}$  model. The single-precision results deviate by several percent after  $J \sim 15$ , where the relative populations are however already below  $10^{-8}$ . The accuracy of single-precision calculations thus appears to be sufficiently for most applications. The PEP parallel and non-parallel runs with double precision give the same results, and also differences to RADEX remain insignificant, reaching  $\sim 10\%$  at the highest level where the relative populations are only  $\sim 10^{-14}$ .

## 4. Results

We used non-LTE radiative transfer runs to produce spectra for different cloud models, analysed these synthetic observations with PEP, and compared the results to the known values of the model clouds. The synthetic spectra were made with the radiative transfer program LOC (Juvela 2020). Section 4.1 examines spherically symmetric models that cover a wide range of optical depths and have non-uniform radial density profiles and partly non-uniform temperatures. In Sect. 4.2 we analyse spectra of more realistic clumps extracted from an MHD simulation of star-forming clouds with supernova-driven turbulence. We use in the tests seven molecular species with the default fractional abundances  $\chi$  of  $10^{-4}$  for CO,  $2 \times 10^{-6}$  for  $^{13}\text{CO}$ ,  $3 \times 10^{-7}$  for  $\text{C}^{18}\text{O}$ ,  $2 \times 10^{-9}$  for  $\text{HCO}^+$ ,  $8 \times 10^{-11}$  for  $\text{H}^{13}\text{CO}^+$ ,  $5 \times 10^{-9}$  for CS,  $10^{-10}$  for  $\text{C}^{34}\text{S}$ , and  $10^{-9}$  for  $\text{N}_2\text{H}^+$  (cf. Navarro-Almaida et al. (2020) and references in Juvela et al. (2022)).  $\text{N}_2\text{H}^+$  is only used in separate tests of the HFS calculations. EPF provides direct column

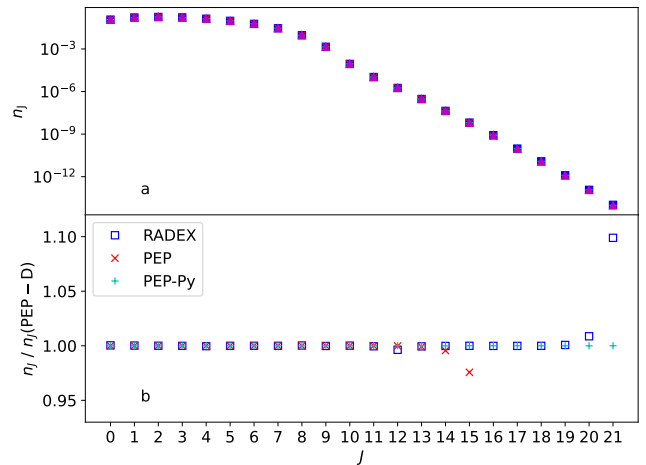


**Fig. 2.** CO level populations for  $T_{\text{kin}} = 70 \text{ K}$ ,  $n(\text{H}_2) = 10^4 \text{ cm}^{-3}$ ,  $N(\text{CO}) = 10^{18} \text{ cm}^{-2}$ , and  $FWHM = 1 \text{ km s}^{-1}$ . The upper frame shows the level populations for all 22 levels ( $J=0-21$ ), and the lower frame shows the level populations relative to the double-precision PEP calculations.

density estimates only for the analysed species. However, to facilitate comparisons between molecules and especially in cases of joint analysis of different species, the results are plotted as functions of  $N(\text{H}_2)$ , using the true values of the fractional abundances  $\chi$ .

### 4.1. Test with spherically symmetric cloud models

#### 4.1.1. Isothermal models

Tests were made with spherically symmetric cloud models. Even when density and  $T_{\text{kin}}$  are constant, the excitation will vary radially. This is in contradiction with the EPF assumptions, and radial density and  $T_{\text{kin}}$  gradients can further affect the accuracy of the EPF analysis. We examined first isothermal clouds where the density profiles correspond to critically stable Bonnor-Ebert (BE) spheres (Ebert 1955; Bonnor 1956) with no large-scale velocity field.

Figure 3 shows an example of the actual photon escape probabilities, excitation temperatures, and line intensities calculated with the LOC program. The cloud is a  $T_{\text{kin}} = 10 \text{ K}$  BE sphere with a mass of  $10 M_{\odot}$ . The  $^{12}\text{CO}$  lines have high optical depths with peak values of 29.4, 49.6, and 26.7 for  $J = 1 - 0$ ,  $J = 2 - 1$ , and  $J = 3 - 2$ , respectively. The radial variation of  $T_{\text{ex}}$  is a factor of two, and the escape probability increases from close to zero at the centre to  $\beta \gtrsim 0.5$  on the cloud surface. EPF cannot be expected to be accurate for models of such high optical depths, but some degree of  $T_{\text{ex}}$  and  $\beta$  gradients exist in all models.

We calculated synthetic spectra towards the model centre, convolved with a Gaussian beam with FWHM equal to one third of the cloud radius,  $FWHM = R_0/3$ . These “observed” spectra were fitted with Gaussians, and the EPF analysis was based on the fitted intensities. Initially  $T_{\text{kin}}$  was fixed to its correct value. EPF gives predictions for the density and the column density, when  $dN/dv$  is converted to column density using the correct line FWHM. The beam-averaged reference values of column density and volume density values were obtained directly from the model cloud. In the line-of-sight (LOS) direction these include the full model volume up to the surface of the BE sphere.

The PEP calculations were performed for a wide range of densities and column densities around the reference values. For

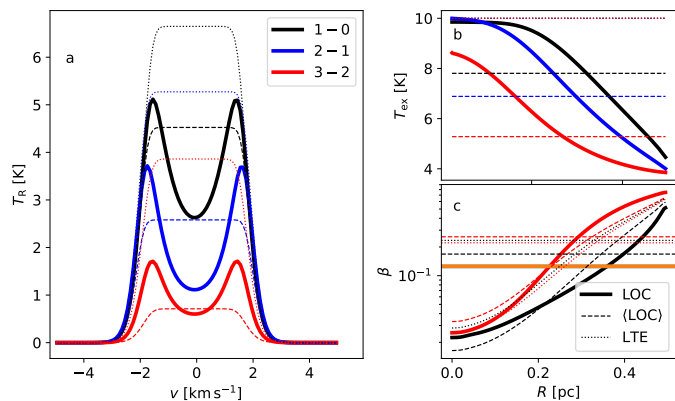


**Fig. 3.** Example of optically thick CO emission from a  $10 M_{\odot}$  BE model with  $T_{\text{kin}}=10$  K. Frame a shows spectra, frame b  $T_{\text{ex}}$  profiles, and frame c the radial variation in the photon escape probability  $\beta$ . Results are shown for full non-LTE calculations with LOC (solid lines), for constant excitation equal to the mean values of the LOC solution (“ $\langle \text{LOC} \rangle$ ”, dashed lines), and for the LTE case at  $T_{\text{kin}}$  (dotted lines). Frames a-b show data for the first three transitions (black, blue, and red, respectively) but, for clarity, frame c includes only the  $J = 1 - 0$  and  $J = 3 - 2$  transitions.

example, the high optical depth of  $^{12}\text{CO}$  lines of the  $M = 2 M_{\odot}$  and  $T_{\text{kin}} = 10$  K model resulted in a highly degenerate solution that was not in contradiction with the reference values but also provided no upper limits for density and column density. The corresponding results for  $^{13}\text{CO}$  are shown in Fig. 4. Each transition constrains the EPF solution to a band of parameter values, the green hatched region showing the area where the line intensity predicted by PEP is within  $\pm 10\%$  of the observed line intensity. The  $n(\text{H}_2)$  values are not constrained but the EPF analysis is mostly consistent with the reference values of density and column density. The combination of the multiple transitions provides more constraints, but for example the combination of  $J = 1 - 0$  and  $J = 4 - 3$  would only reject densities above the  $n(\text{H}_2)$  reference value.

The above  $^{12}\text{CO}$  and  $^{13}\text{CO}$  spectra were not optically thin and were either flat-topped or with self-absorption dips (cf. Sect. C.1). The CS and  $\text{C}^{34}\text{S}$  results for the same cloud model are shown in Fig. 5. The CS  $J = 2 - 1$  spectrum has a small dip in the line centre, but the other spectra are nearly Gaussian. The predicted bands of  $n(\text{H}_2)$  and column density are narrow, especially for  $\text{C}^{34}\text{S}$ . They are partly inconsistent with each other (e.g. CS  $J = 3 - 2$  vs.  $J = 5 - 4$ ), but for example the combination of  $\text{C}^{34}\text{S}$   $J = 2 - 1$  and  $J = 5 - 4$  would constrain the solution close to the reference solution.

Corresponding results for  $^{12}\text{CO}$  and  $^{13}\text{CO}$  spectra from the  $10 M_{\odot}$  cloud at  $T_{\text{kin}}=20$  K are shown in Appendix C.1 (Fig. C.6). This shows similarly some discrepancy between the isotopomers, even with perfect knowledge of the fractional abundances. For example, the combination of  $^{13}\text{CO}$   $J = 1 - 0$  and  $J = 4 - 3$  lines would result in a nearly unique solution but with  $\sim 0.2$  dex errors, underestimating the  $n(\text{H}_2)$  and overestimating column density. Of other combinations, CO(3-2) and  $^{13}\text{CO}(1-0)$  would indicate at least 0.5 dex too low density and too high column density.

We examined the  $\chi^2$  values for combinations of multiple transitions, using BE models with masses  $M=0.2, 5,$  and  $10 M_{\odot}$  and kinetic temperatures  $T_{\text{kin}}=10, 20,$  and  $50$  K. The observations are assumed to have 10% uncertainty, but no noise is added to the input spectra. The fit quality is measured by a  $\chi^2$  value that

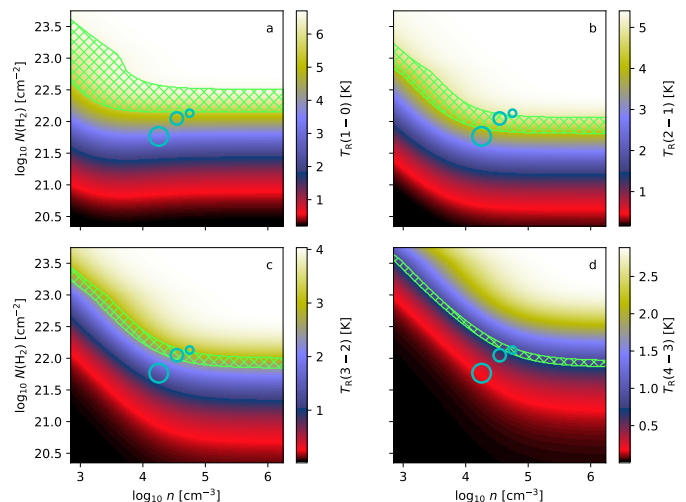


**Fig. 4.** PEP results for  $^{13}\text{CO}$  spectra towards a BE sphere with  $T_{\text{kin}} = 10$  K and  $M = 2 M_{\odot}$ . The colour scale shows the predicted line intensities as a function of volume and column density. In the green hatched areas PEP predictions are within 10% of the observed line intensities. The circles indicate the reference cloud parameters for the central LOS (small circle), the beam average with  $FWHM = R_0/3$  (middle circle corresponding to the beam in the synthetic observations) and for  $FWHM = R_0$  (large circle).

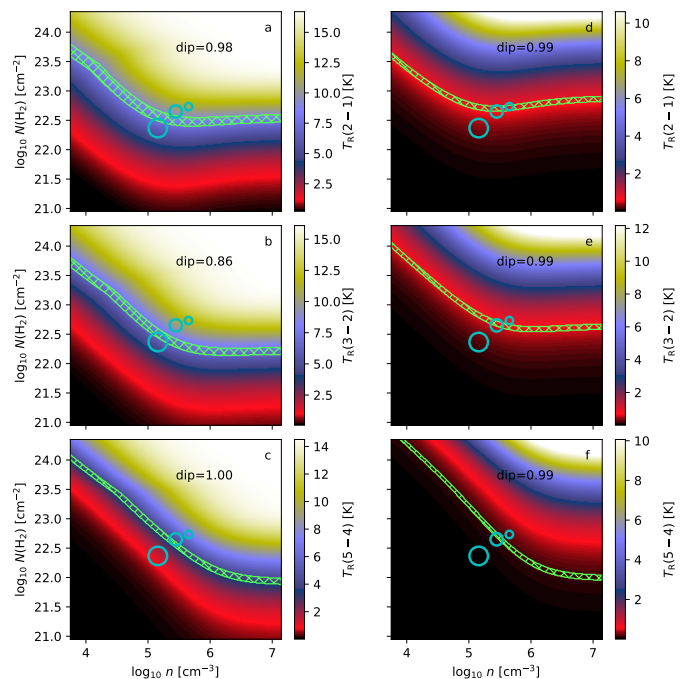


**Fig. 5.** PEP analysis of CS (left frames) and  $\text{C}^{34}\text{S}$  (right) line intensities. The plotted symbols are as in the previous figures. The cloud model is the same as in the previous figures, with  $M = 2 M_{\odot}$  and  $T_{\text{kin}}=20$  K. Each frame quotes the depth of the possible self-absorption dip as the line intensity at the line centre divided by the maximum intensity.

is the average of the individual transitions. For observations with 10% noise  $\chi^2$  would thus be expected to be of the order of one.

The value of  $T_{\text{kin}}$  was initially fixed to its correct value. Figure 6 shows  $\chi^2$  values for  $^{13}\text{CO}$ . To resolve the  $\chi^2$  minimum, the number of data points was 300 along both the density and

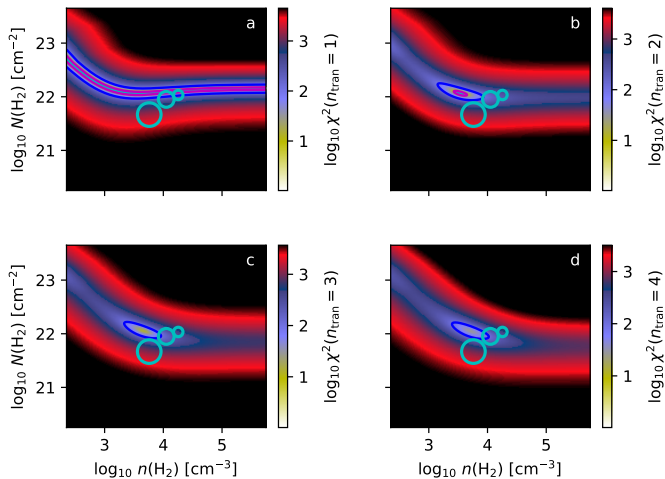


**Fig. 6.** Combined  $\chi^2$  values in PEP analysis of  $^{13}\text{CO}$  spectra. The cloud model an isothermal BE sphere with  $M = 10 M_{\odot}$  and  $T_{\text{kin}} = 20\text{ K}$ . The frames a-d correspond, respectively, to the combinations of the 1-4 first rotational transitions. The circles indicate the reference values towards its centre (smallest circle), averaged over a  $FWHM = R_0/3$  beam (middle circle that corresponds to the synthetic observations), and averaged over a  $FWHM = R_0$  beam (largest circle).

column density axes. The addition of a second transition partly breaks the degeneracy, but further transitions provide only little improvement. The  $\chi^2$  minimum is slightly above the correct  $N(\text{H}_2)$  value but almost 0.5 dex below the reference density. The dense part of the cloud emits more strongly, especially if outer parts fall below the critical density. Therefore, one might expect EPF to overestimate the reference density. However, this is not what is seen in Fig. 6.

Figure 7 summarises the results for seven molecules in the case of the  $M = 0.5 M_{\odot}$  and  $T_{\text{kin}} = 20\text{ K}$  model. The  $\chi^2$  values are in some cases much higher at the location of the reference parameters  $n(\text{H}_2)$  and  $N(\text{H}_2)$  than at the  $\chi^2$  minimum (e.g. for  $\text{C}^{34}\text{S}$  and  $\text{H}^{13}\text{CO}^+$ ). The EPF analysis would thus reject the correct solution with an apparent high level of confidence (if the reference solution can be considered the correct one). Even the minimum  $\chi^2$  values can be high, up to  $\chi^2 \sim 100$ , when the evidence of the individual transitions is contradictory. The previous figures already showed (e.g. Fig. 5) that  $\chi^2$  can increase very rapidly when one moves outside the narrow valley of the lowest  $\chi^2$  values.

Figure 7 shows that in most cases the column density is correct to within a factor of a few. The main exception is  $\text{HCO}^+$ . Based on the spectral profiles shown in Appendix C.1, this could be due to strong self-absorption. Although Fig. 7 suggest order of magnitude errors for  $\text{HCO}^+$ , the high optical depth also means a larger degree of degeneracy, where the global  $\chi^2$  minimum can be located far from the reference parameter values, the latter still not being rejected with any high significance. Indeed, for  $\text{HCO}^+$  the  $\chi^2$  values are almost the same at the reference position, indicating that the parameters are not well constrained. The same applies to  $^{12}\text{CO}$  and  $^{13}\text{CO}$ , although there the nominal parameter uncertainties tend to be smaller. While EPF cannot be expected to be accurate for optically thick lines, the same applies to some extent to any radiative transfer analysis (van der Tak et al. 2007; Asensio Ramos & Elitzur 2018). For the less optically thick species, the column density may be correct to within a factor of two, but, as implied by previous  $\chi^2$  images, the den-

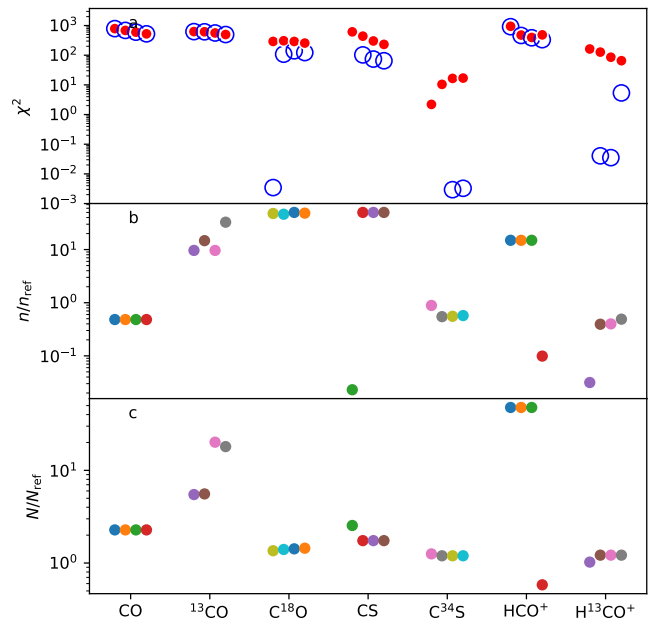


**Fig. 7.** Results for seven molecules observed towards an isothermal BE sphere with  $M = 0.5 M_{\odot}$  and  $T_{\text{kin}} = 20\text{ K}$ . Frame a shows the minimum  $\chi^2$  value (blue open circles) and  $\chi^2$  value for the reference density and column density (red filled circles). Frames b and c, respectively, show the ratio of density and column density values at the  $\chi^2$  minimum relative to the reference values. Each molecule is plotted with four markers that, from left to right, correspond to the combination of 1-4 lowest transitions.

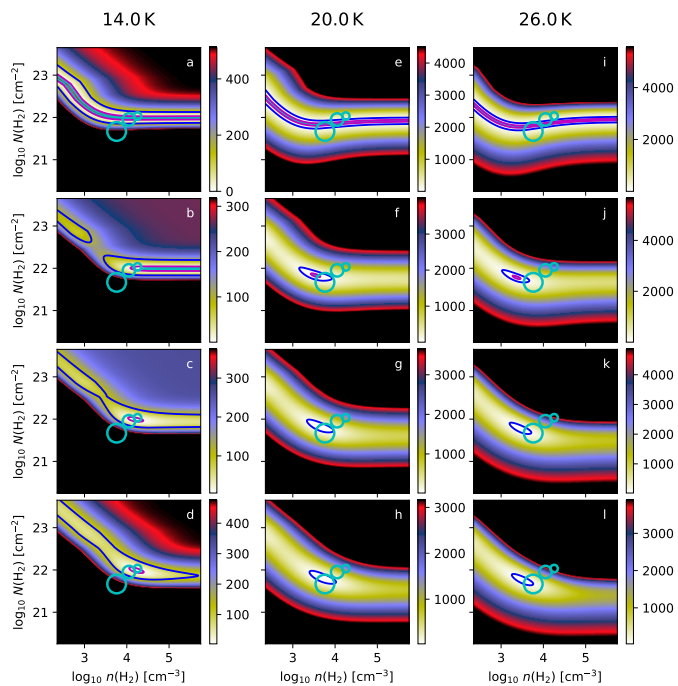
sity remains unconstrained. Appendix C.2 includes further plots for other cloud models, where higher  $T_{\text{kin}}$  tends to result in more accurate results.

Figure 8 shows an example where  $^{13}\text{CO}$  spectra are analysed using  $T_{\text{kin}}$  that is 30% below or above the correct value. Depending on the transitions used, such  $T_{\text{kin}}$  uncertainty can result in up to one dex change in the estimated density. In this example the 30% underestimation of  $T_{\text{kin}}$  actually gives partly the best match to reference  $n(\text{H}_2)$  and  $N(\text{H}_2)$  values. Higher  $T_{\text{kin}}$  decreases the estimated  $N(\text{H}_2)$ , slightly less than 0.5 dex for the  $\pm 30\%$   $T_{\text{kin}}$  change.

Figure 9 shows results for the same model, varying  $T_{\text{kin}}$  around the correct value. The  $\chi^2(T_{\text{kin}})$  does not have a clear minimum, but the estimated column density remains correct to within a factor of two over the plotted range, with only slightly larger maximum error (and negative bias) for the density.

The situation is very different for the denser cloud with  $M = 2 M_{\odot}$  (Fig. 10). The  $\chi^2(T_{\text{kin}})$  reaches the minimum  $\sim 2\text{ K}$  above the true temperature, at which point  $N$  is correct to within a factor of two but the density is poorly constrained. As  $T_{\text{kin}}$  increases, the  $n(\text{H}_2)$  estimate drifts from the upper limit to the bottom limit of the probed range. This reflects the almost completely degeneracy of the models with respect to  $n(\text{H}_2)$ . If the temperature were fixed to the correct value of  $T_{\text{kin}} = 20\text{ K}$ , the column density would be strongly overestimated, as suggested by Fig. 7. The plot of the  $\chi^2$  planes are included in appendix (Fig. C.11). That shows that, apart from the +30%  $T_{\text{kin}}$  value, the spectra are at the limit of saturation, which results in the observed large errors.

A more positive example  $\text{C}^{34}\text{S}$  spectra is shown in Fig. 11, where the  $\chi^2$  minimum is reached at the correct temperature, with accurate predictions for both  $n(\text{H}_2)$  and the column density.



**Fig. 8.** Plots of  $\chi^2$  in the EPF analysis of  $^{13}\text{CO}$  lines. The analysis used three  $T_{\text{kin}}$  temperatures, as listed above each column of frames. The cloud model is an isothermal BE sphere with  $M = 10 M_{\odot}$  and  $T_{\text{kin}} = 20$  K. First row shows the analysis of the  $J = 1 - 0$  lines, and each subsequent row adds one further rotational transition. The contours are drawn at  $\chi^2$  levels of 1 (red), 2 (cyan), 10 (magenta), and 100 (blue contour). In order of increasing size, the circles indicate the reference density and column density values towards the model centre, averaged over a  $FWHM = R_0/3$  beam (used for the synthetic observations), and averaged over a  $FWHM = R_0$  beam.

However, even in this case, if  $T_{\text{kin}}$  were fixed to just 1 K higher value, the errors could approach one order of magnitude.

In the above tests the  $\pm 30\%$  range of  $T_{\text{kin}}$  was sampled with 100 points (e.g.  $\Delta T_{\text{kin}} = 0.025$  K for  $T_{\text{kin}} = 10$  K). Given the reference values for  $n(\text{H}_2)$  and  $N(\text{H}_2)$ , our PEP calculations covered parameter ranges from 50 times lower to 50 times higher values, using a grid of  $500 \times 500$  points. In spite of the fine grid, the aliasing is still visible as saw-tooth pattern, especially in Fig. 11. This could be avoided by interpolation, but is shown as a reminder of the parameter degeneracies and the resulting challenging shape of the  $\chi^2$  surface.

When the analysis includes multiple species, the result depend on the assumed fractional abundances. Figure 12 shows an example of the combination of CS and  $\text{C}^{34}\text{S}$  observations with  $\pm 50\%$  errors in the assumed  $\text{C}^{34}\text{S}$  abundance. Density is constrained only if higher transitions are included. The changes in the fractional abundance cause 0.5 dex shift in column density, an effect that is larger than the direct error in the  $\text{C}^{34}\text{S}$  abundance. Appendix C.2 shows further examples for the same lines at  $T_{\text{kin}} = 10$  K or  $T_{\text{kin}} = 20$  K, generally with similarly small effects on the parameter estimates.

#### 4.1.2. Non-isothermal models

As the final exercise with the 1D models, we examined the effect of radial  $T_{\text{kin}}$  gradients. The mass-weighted mean  $T_{\text{kin}}$  was set to 10, 20, or 50 K, and the density profile was calculate for the corresponding isothermal model. The temperatures were then mod-

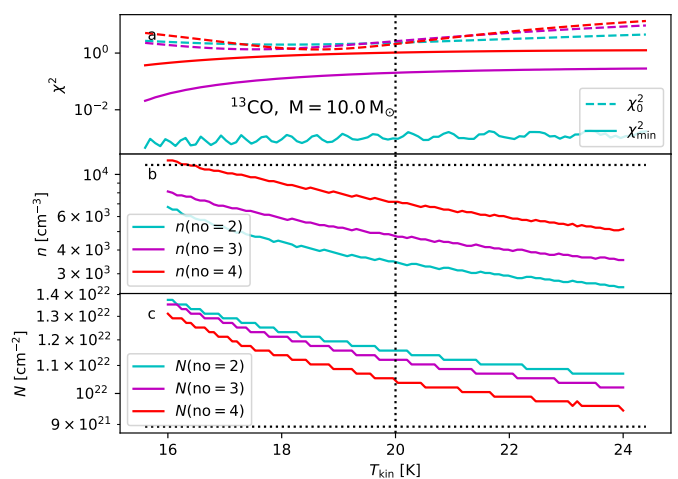


**Fig. 9.** Change in the minimum- $\chi^2$  PEP solution for  $^{13}\text{CO}$  spectra as a function of  $T_{\text{kin}}$ . The model is a  $10 M_{\odot}$  BE sphere with  $T_{\text{kin}} = 20$  K. Frame a shows the minimum value of  $\chi^2$  (solid lines) and the  $\chi^2$  value for the reference parameter values (dashed lines). Frame b shows the predicted density and frame c the predicted column density. The cyan, magenta, and red colours correspond, respectively, to the analysis using two, three, or four transitions.

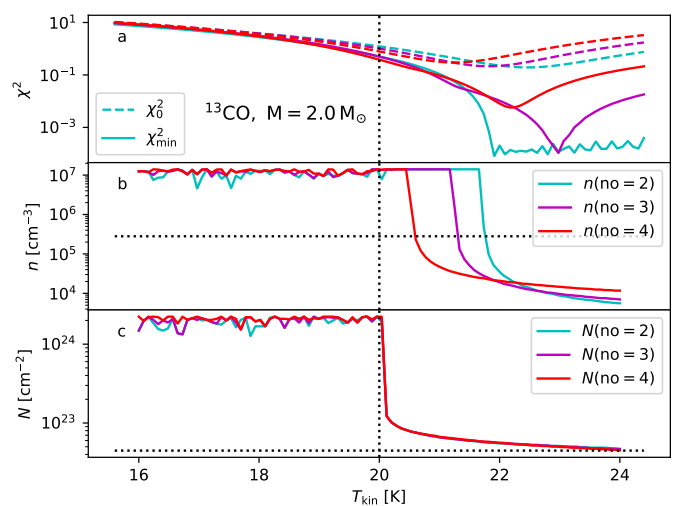
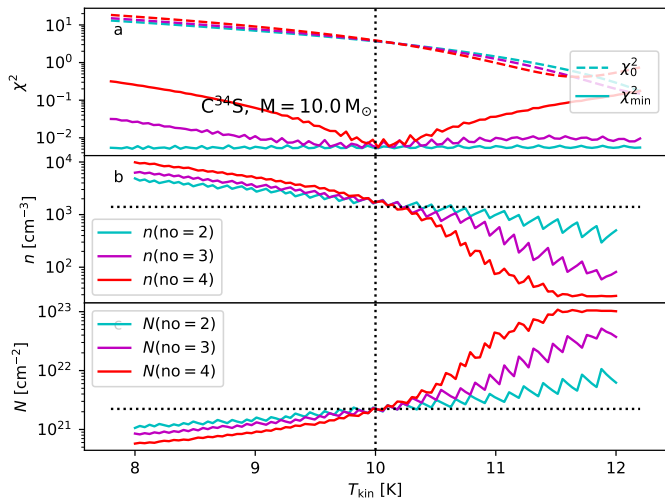


**Fig. 10.** As Fig. 9 but for the synthetic  $^{13}\text{CO}$  observations of the  $M = 2 M_{\odot}$  and  $T_{\text{kin}} = 20$  K model.

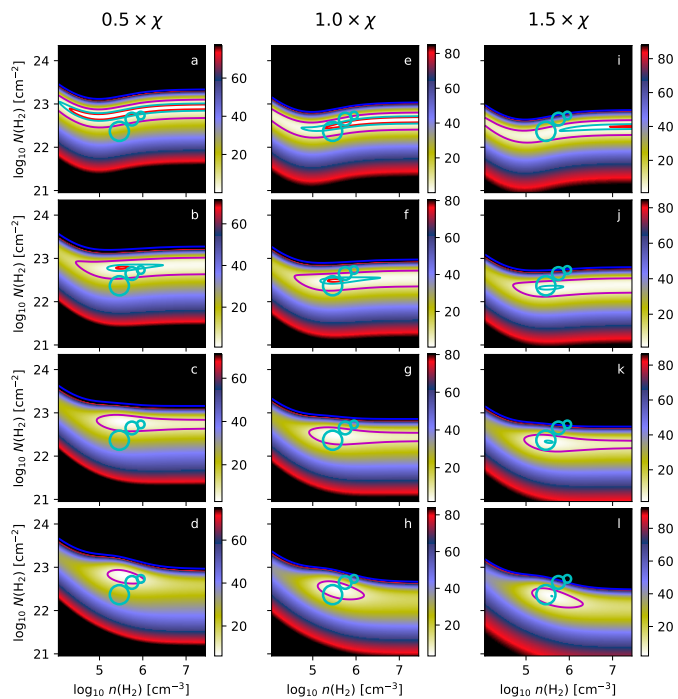
ified to have a constant positive or negative gradient. The total temperature variation is 30% of  $\langle T_{\text{kin}} \rangle$ , but the mass-weighted average temperature  $\langle T_{\text{kin}} \rangle$  was kept at the original value.

Figure 13 shows results for  $^{13}\text{CO}$  spectra from a model with  $T_{\text{kin}}$  increasing outwards, for observations with a Gaussian beam of  $FWHM = R_0/3$ . Apart from the temperature gradient, the situation is the same as in Sect. 4.1.1. The line intensities predict column densities that are below the reference value, although the change is less than 0.2 dex. The case with  $T_{\text{kin}}$  decreasing outwards is shown in Fig. 14. The  $^{13}\text{CO}$   $J = 1 - 0$  transition is now matched over a much wider range of parameters, while higher transitions now prefer column density that is 0.2 dex above the reference value (at the same density) or 0.4 dex above the previous case with  $T_{\text{kin}}$  increasing outwards.

Appendix C.3 shows two further examples with radial  $T_{\text{kin}}$  gradients for the combination of CS and  $\text{C}^{34}\text{S}$  spectra. Overall,



**Fig. 11.** As Fig. 9 but for  $C^{34}S$  observations of the  $M = 10 M_{\odot}$ ,  $T_{\text{kin}} = 10$  K model.



**Fig. 12.** Estimated  $\chi^2$  for combined CS and  $C^{34}S$  observations of a BE sphere with  $M = 0.5 M_{\odot}$  and  $T_{\text{kin}} = 10$  K. The columns correspond to the assumed  $C^{34}S$  abundances (correct and with  $\pm 50\%$  errors). The first row shows results for the  $J = 1 - 0$  line, and each subsequent row adds one more rotational transition.

the temperature gradients introduce only modest changes compared to the isothermal cases.

Figures 15 and 16 show a more extreme example,  $^{12}CO$  observations of the  $M = 2 M_{\odot}$  model with  $T_{\text{kin}} = 10$  K. As shown in Appendix C.1, the corresponding  $^{12}CO$  spectra of isothermal models are flat-topped but do not yet show any self-absorption dips. However, when  $T_{\text{kin}}$  increases outwards (Fig. 15), the observations fall in the saturated region, and only the optically less thick  $J = 4 - 3$  transition is able to constrain the combination of density and column density values. When the temperature gra-

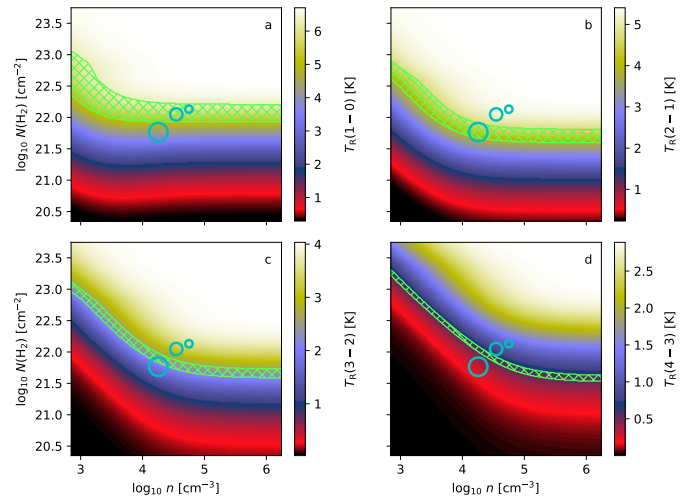


**Fig. 13.** Results for  $^{13}CO$  spectra of the  $M = 2 M_{\odot}$  BE model with  $\langle T_{\text{kin}} \rangle = 10$  K. The case is similar to that of Fig. 4 except that  $T_{\text{kin}}$  increases outwards.

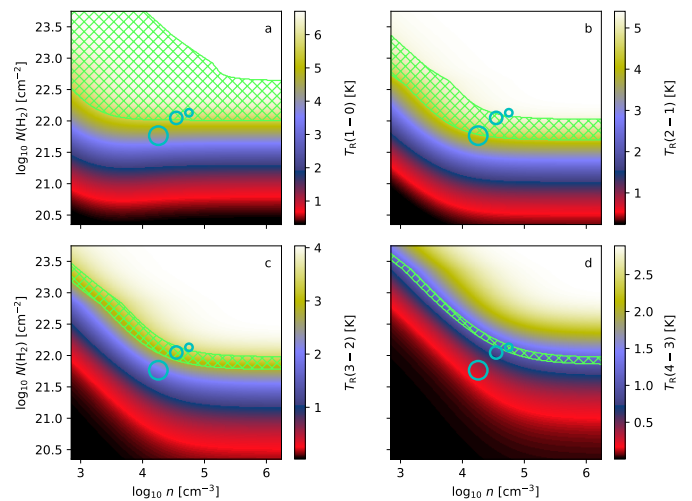


**Fig. 14.** As Fig. 13 but with  $T_{\text{kin}}$  decreasing outwards.

dent is reversed (Fig. 16), the results have the appearance of  $n(H_2)$  and the column density being better constrained but the values are in reality significantly underestimated.

#### 4.2. Clumps from 3D MHD cloud simulation

As more realistic examples of sources, we examined clumps extracted from a  $(250 \text{ pc})^3$  MHD simulation of supernova-driven turbulence (Padoan et al. 2016). The mean density of hydrogen nuclei in the model is  $5 \text{ cm}^{-3}$ , but turbulence and self-gravity increase the maximum values to  $\sim 10^7 \text{ cm}^{-3}$  in the selected snapshot. The hierarchical discretisation reaches a maximum resolution of 7.6 mpc.

The simulation provides the density and velocity fields. The velocity dispersion inside the cells was estimated from the dispersion between neighbouring cells ( $2^3$  cells per octree parent cells, scaled down by a factor 1.5) and this is added to the thermal line broadening. Because the MHD simulation does not provide gas kinetic temperatures  $T_{\text{kin}}$ , we used dust temperatures from separate continuum radiative transfer calculations (cf. Ju-

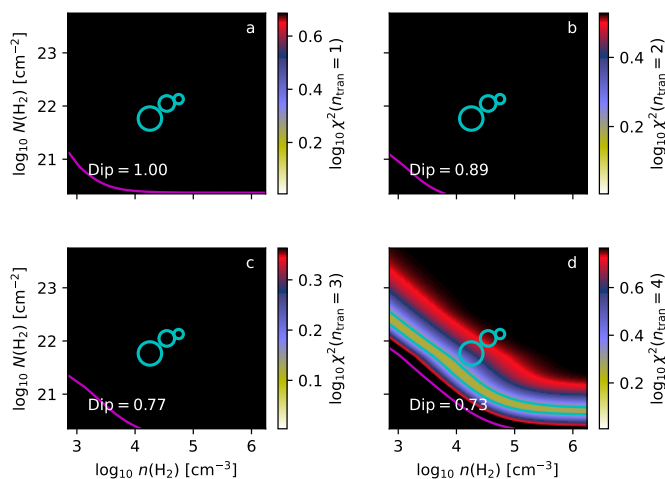


**Fig. 15.** Values of  $\chi^2$  as function of density and column density for a non-isothermal  $2M_{\odot}$  model with  $\langle T_{\text{kin}} \rangle = 10$  K and  $T_{\text{kin}}$  increasing outwards. Frame a is based on the fit to  $^{12}\text{CO } J = 1 - 0$  spectra, and each subsequent frame includes to the analysis one further rotational level.

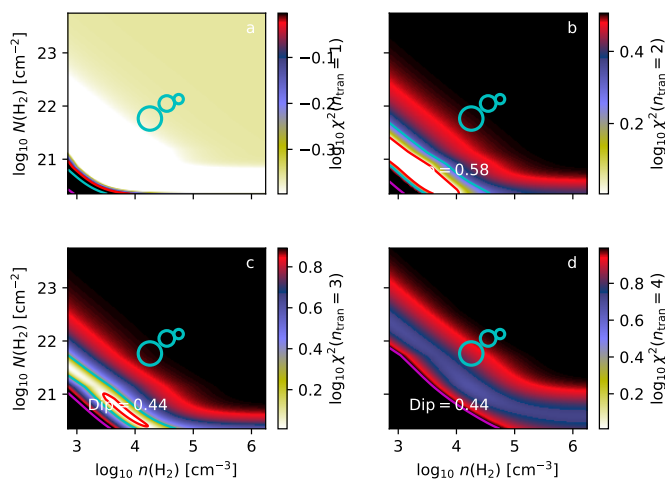


**Fig. 16.** As Fig. 15 but with  $T_{\text{kin}}$  decreasing outwards in the model cloud.

vela et al. 2022) as the proxy for  $T_{\text{kin}}$ . Gas temperature follows dust temperature accurately only at densities  $n(\text{H}_2) \gtrsim 10^5 \text{ cm}^{-3}$  (Goldsmith 2001; Juvela & Ysard 2011). However, the procedure gives a realistic temperature structure that extends from typical  $\sim 20$  K at low densities to less than 10 K in dense cores. The continuum modelling includes radiation of the stars that have formed in the MHD simulation. This increases further the complexity of the temperature field, 0.25% of the cells reaching values above  $T_{\text{kin}} \sim 30$  K.

In the absence of chemical modelling, we used constant fractional abundances or, alternatively, values further set based on the density,  $\chi = n(\text{H}_2)^{2.45} / [3.0 \times 10^8 + n(\text{H}_2)^{2.45}] \chi_0$ , with the  $\chi_0$  values listed at the beginning of Sect. 4. The abundance becomes small below  $n(\text{H}_2) \sim 2 \times 10^3 \text{ cm}^{-3}$ , thus affecting more lines of low critical density (Shirley 2015).

We calculated  $^{13}\text{CO}$  spectral line maps for the full MHD model, convolved the line area map to 0.25 pc resolution, and selected peaks with the integrated  $J = 2 - 1$  line intensity above  $6 \text{ K km s}^{-1}$ . For each peak, we located the maximum volume

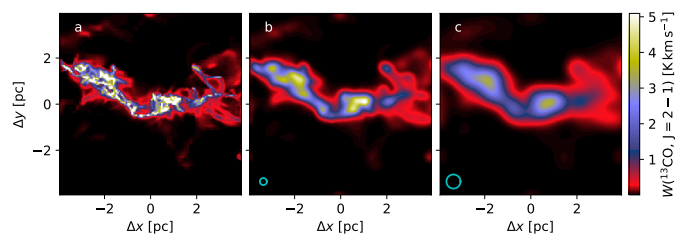


**Fig. 17.** Example of a clump extracted from the MHD model. The frames show the  $^{13}\text{CO}(2-1)$  line-area maps at the full resolution (frame a) and for observations with  $FWHM=0.31$  pc (frame b) and  $FWHM=0.61$  pc (frame c) beam sizes. The fractional abundance is spatially constant.

density along the line of sight, and resampled the data for the surrounding  $(7.9 \text{ pc})^3$  volume onto a Cartesian grid with a 0.061 pc cell size. After rejecting sources close to the edges of the MHD cube and three sources with multiple velocity components, the final sample contains 55 targets that are in the following called clumps.

The LOC program was used to calculate synthetic non-LTE spectra for  $^{12}\text{CO}$ ,  $^{13}\text{CO}$ ,  $\text{C}^{18}\text{O}$ ,  $\text{CS}$ ,  $\text{C}^{34}\text{S}$ ,  $\text{HCO}^+$ , and  $\text{H}^{13}\text{CO}^+$ , using the first three rotational transitions for the EPF analysis. Each clump was observed with the beam sizes of  $FWHM=0.31$ , 0.61, and 1.22 parsecs (5, 10, or 20 model cells), and the parameters of Gaussians fits to the line profiles were used as inputs for the EPF analysis.

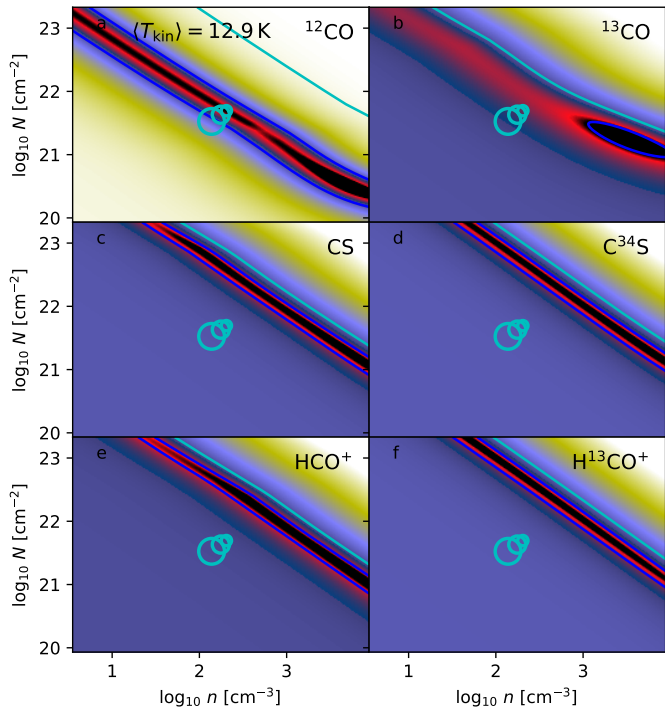
We extracted reference values from the model cubes. The mean densities and mean column densities were obtained by weighting the data with the same Gaussian beams as in the synthetic observations. The mean temperature  $\langle T_{\text{kin}} \rangle$  was weighted by both the beam and the density. When the fractional abundances were not constant, alternative values of  $\langle n(\text{H}_2) \rangle$ ,  $\langle N(\text{H}_2) \rangle$ , and  $\langle T_{\text{kin}} \rangle$  were obtained by further weighting the data by the fractional abundances. A large part of each model cube is filled by low-density gas will small contribution to the emission. Therefore, in the constant-abundance case the reference density can be expected to be lower than the mean density derived from the observed spectra. The difference should be smaller in the case of variable abundances, because the abundance weighting also reduces the contribution of low-density cells with  $n(\text{H}_2) \lesssim 10^3 \text{ cm}^{-3}$ .

Figure 17 shows  $^{13}\text{CO}(2-1)$  maps for one clump and different beam sizes. The field shows a typical filamentary structure that, when observed with a large beam (e.g.  $FWHM=0.61$  pc or  $FWHM=1.22$  pc), can lead to low beam filling. We analyse for each clump only one line of sight that corresponds to the maximum of the  $^{13}\text{CO } J = 2 - 1$  line area map observed with the  $FWHM=0.31$  pc beam.

Figure 18 shows results for one clump with constant fractional abundances and the intermediate beam size. The EPF analysis uses a kinetic temperature equal to  $\langle T_{\text{kin}} \rangle$ . The  $\chi^2$  values are averages over the first three rotational transitions and are shown for  $^{12}\text{CO}$ ,  $^{13}\text{CO}$ ,  $\text{CS}$ ,  $\text{C}^{34}\text{S}$ ,  $\text{HCO}^+$ , and  $\text{H}^{13}\text{CO}^+$ . The beam-weighted reference values  $\langle n(\text{H}_2) \rangle$  and  $\langle N(\text{H}_2) \rangle$  are also shown.

The EPF estimates of the density and column density are still strongly degenerate. Only  $^{13}\text{CO}$  results show a clear localised minimum, although more than an order of magnitude above the expected density  $\langle n(\text{H}_2) \rangle$ . That is caused by the reference value of  $\langle n(\text{H}_2) \rangle$  including low-density gas with little contribution to the observed spectra. Even if the reference value were an order of magnitude higher, to match the predicted volume density, the





**Fig. 18.** PEP results for a MHD clump, using the  $T_{\text{kin}}$  value given in frame a. Each frame shows  $\chi^2$  for one molecule and its first three rotational transitions. The cyan circles indicate the beam-averaged model mean densities and column densities (sizes in order of increasing FWHM). The  $\chi^2$  values are based on the medium beam size. The blue, cyan, magenta, and red contours correspond to  $\chi^2=1, 2, 10,$  and  $100$ .

column density would still be overestimated by almost 0.5 dex. That density would be almost 1 dex above the EPF prediction based on the  $^{12}\text{CO}$  lines. A 20% change in the assumed  $T_{\text{kin}}$  would change these results only marginally.

In the variable-abundance case the reference value for  $n(\text{H}_2)$  is indeed about one order of magnitude higher (Fig. 19), in better agreement with the EPF predictions based on the  $^{13}\text{CO}$  lines. However, the reference values are still at  $\sim 0.3$  dex lower density and  $\sim 0.2$  dex higher column density. For  $^{12}\text{CO}$  the reference values are clearly above the EPF predictions, which show a narrow valley of low  $\chi^2$  values. For the other molecules the reference values are located only very slightly below the  $\chi^2$  valley.

The plots show very elongated regions of low  $\chi^2$  values. Therefore, instead of the difference between the reference parameter values  $r_{\text{ref}}$  and the  $\chi^2$  minimum of EPF estimates, we concentrate on the distance between  $r_{\text{ref}}$  and the nearest point along the  $\chi^2$  valley. We searched the minimum  $\chi_{\text{line}}^2$  along the  $(\Delta \log n(\text{H}_2), \Delta \log N(\text{H}_2))=(1,1)$  direction. That was then replaced with the final position  $r_{\text{est}}$  that is the closest position to  $r_{\text{ref}}$  where  $\chi^2 \leq \chi_{\text{line}}^2$ , where all distances are measured in terms of density and column density logarithms. The distance between  $r_{\text{ref}}$  and  $r_{\text{est}}$  is thus only a lower limit for the distance between  $r_{\text{ref}}$  and the global  $\chi^2$  minimum. When  $\chi^2$  varies little along the  $\chi^2$  valley, it is still a good measure for the discrepancy between the EPF predictions and the reference values.

Figure 20 shows the density and column density ratios between the  $r_{\text{ref}}$  and  $r_{\text{est}}$  positions, using the notation  $N_{\text{est}}/N_{\text{ref}} = N(r_{\text{est}})/N(r_{\text{ref}})$ . The data consist of  $^{12}\text{CO}$  observations with the  $\text{FWHM}=0.61$  pc beam size. The reference values  $r_{\text{ref}}$  are again

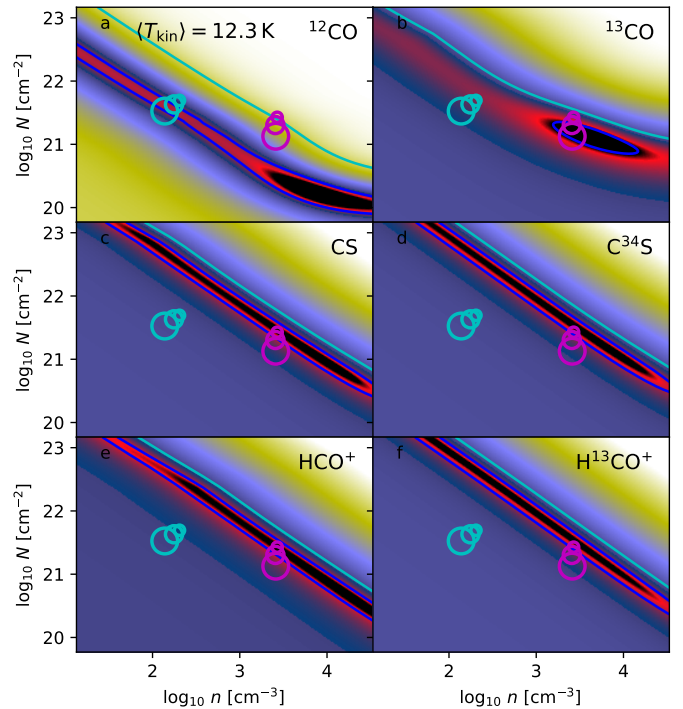


**Fig. 19.** As Fig. 18 but for a model with density-dependent abundances. The reference values are shown without (cyan circles) and with the weighting by fractional abundances (magenta circles). The circle sizes correspond to the three beam sizes, in order of increasing FWHM. The  $\chi^2$  values correspond to observations with the intermediate beam size.

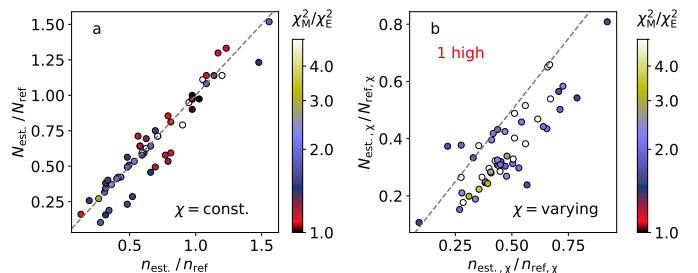


**Fig. 20.** Comparison of EPF estimates and reference values for  $^{12}\text{CO}$  spectra observed with the intermediate beam size. Frames a and b correspond, respectively, to the constant and variable abundance cases. The marker colours show the  $\chi^2$  ratio between the  $r_{\text{ref}}$  and  $r_{\text{est}}$  positions. In frame b the red text refers to one outlier with ratios larger than ten.

averages from the model cubes weighted by the beam and, in the case of varying abundances, also by the abundance  $\chi$ .

As suggested by Fig. 18, in the case of  $^{12}\text{CO}$  the bias is not very large even in the constant-abundance case, with  $0.3 \lesssim n_{\text{est}}/n_{\text{ref}} \lesssim 1.6$  and  $0.2 \lesssim N_{\text{est}}/N_{\text{ref}} \lesssim 1.5$ . One should also remember that the best definition of the reference density remains uncertain. In the variable- $\chi$  case the EPF analysis of  $^{12}\text{CO}$  underestimates the reference values typically by a factor of two, in agreement with Fig. 19.

We also analysed  $^{12}\text{CO}$  observations for models, where the densities were increased by an ad hoc factor of five (figures not shown). The results are qualitatively similar to Fig. 20, except that for seven cores the  $^{12}\text{CO}$  line intensities fall into a degenerate region due to line saturation. Thus, instead of the one out-

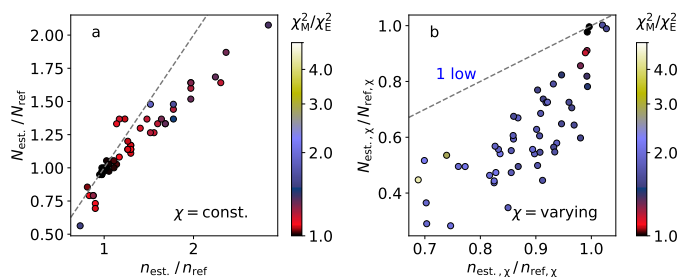


**Fig. 21.** As Fig. 20 but for  $^{13}\text{CO}$  observations. In blue text in frame b refers to one outlier with both ratios below 0.05.

lier in Fig. 20, there are now more outliers with high  $n(\text{H}_2)$  and  $N(\text{H}_2)$  values (seven for constant- $\chi$  and 14 for the variable- $\chi$  case). In those cases the global  $\chi^2$  minimum may be located at much higher  $n(\text{H}_2)$  and  $N(\text{H}_2)$  values but  $\chi^2$  being only slightly lower than at the  $r_{\text{ref}}$  position. Thus, in the case of these outliers, EPF is not able to constrain the parameters but also is not in strong contradiction with the reference values.

The results for  $^{13}\text{CO}$  spectra are shown in Fig. 21. For constant fractional abundances, the  $n(\text{H}_2)$  and  $N(\text{H}_2)$  estimates are  $\sim 30\%$  above the reference values, and the largest discrepancies exceed a factor of two. In the case of variable  $\chi$ , the reference values are underestimated, especially in column density. Figure 21b contains one outlier where the  $n(\text{H}_2)$  and column density ratios are exceptionally low. The source appears normal, except for having a low temperature  $\langle T_{\text{kin}} \rangle = 9.6 \text{ K}$ . If the model densities were increased by a factor of five (not shown), there are no outliers. The  $^{13}\text{CO}$  parameter estimates are closer to the reference values in the constant- $\chi$  case, while in the variable- $\chi$  case column density estimates are on average 45% of the reference values.

Also other molecules tend to show larger discrepancy in the constant- $\chi$  case, partly because the reference value of  $n(\text{H}_2)$  underestimates the density of the emitting (sub)region (Appendix D). The variable- $\chi$  results are consistent with the reference values to within a factor of two, with occasional outliers. The main feature is the correlation between the density and column density discrepancies (distance between  $r_{\text{est}}$  and  $r_{\text{ref}}$ ). This is not caused directly by our definition of  $r_{\text{est}}$ , which could be located in any direction from  $r_{\text{ref}}$ , as long as its  $\chi^2$  values is equal or smaller than the minimum value along the initial diagonal search direction.

## 5. Discussion

We have presented PEP, a parallel program for EPF line calculations. Synthetic spectral line observations were used to investigate the differences between the EPF predictions and the actual source parameters. The parameters  $p_i$  are the volume density  $n(\text{H}_2)$ , the column density  $N$  of the examined species (together with the assumed line width  $FWHM$ ), and the kinetic temperature  $T_{\text{kin}}$ . We have omitted observational errors and concentrated on the model errors caused by the assumptions inherent to the EPF analysis.

### 5.1. Spherically symmetric models

The spherically symmetric 1D models break the EPF assumptions due to radial variations in the photon escape probability (cf. Fig. 3), the effects being enhanced by non-uniform density

and  $T_{\text{kin}}$ . For optically thick lines, these lead to self-absorption that cannot be modelled with EPF and usually results in biased results or little constraints on the source parameters. Even in the absence of strong self absorption, each line probes preferentially different cloud layers, according to its optical depth.

To constrain all parameters  $p_i$ , it is in principle better to combine observations of lines with different (lower) optical depths and critical densities (Tunnard & Greve 2016; Roueff et al. 2024). In the tests the degeneracy was sometimes reduced by combining multiple transitions of the same species, such as the case of  $\text{C}^{34}\text{S}$  in Fig. 5. However, it was also seen that different transitions may not all be consistent with the same solution (e.g.  $^{13}\text{CO}$  in Fig. C.6). Combined with parameter degeneracies, this can result in an apparent match with observations but with clearly erroneous parameter values. When observations of different species are combined, incorrect estimates of the fractional abundances clearly bias the results or, if that uncertainty is taken into account, will weaken the constraints on the cloud parameters.

The reference values of mean density and column density were relatively well defined, thanks to the clear outer boundary of the BE spheres. In tests with the correct  $T_{\text{kin}}$  values, the combination of  $n(\text{H}_2)$  and  $N(\text{H}_2)$  (in plots corresponding to the true fractional abundance of the species) was generally constrained to a narrow band, and the individual parameters could not be determined with high accuracy (such as in the tests conducted with the  $^{12}\text{CO}$  and  $^{13}\text{CO}$  lines). When lines were not optically thick, the column density estimates (at the  $\chi^2$  minimum) were mostly within a factor of two of the correct value (Fig. 7 and Figs. C.7-C.10). However, also much larger errors can occur and even at moderate optical depths.

When temperature was included as a free parameter, correct values of  $T_{\text{kin}}$ ,  $n(\text{H}_2)$ , and column density could be recovered accurately only in the best cases. The examples showed that a 1 K error in  $T_{\text{kin}}$  could result even in a factor of several change in the other parameters (Fig. 11). The tests did not include observational noise, but those large errors might well be realised due to noise in intensity measurements. For the optically more thick  $^{13}\text{CO}$  lines the  $T_{\text{kin}}$  estimates were generally biased or  $T_{\text{kin}}$  remained unconstrained. In some cases the  $n(\text{H}_2)$  and column density estimates were quite insensitive to temperature (Fig. 9). In other cases, especially due to line saturation, a less than degree error in temperature could result in an order of magnitude change in the other predicted parameters (Fig. 10). The analysis of multiple species and transitions of different optical depths should either confirm the correct solution or reveal the true uncertainty of the estimates.

### 5.2. Clumps extracted from MHD simulations

The MHD simulation provided more realistic test cases with complex density and temperature structures and the added effects of different velocity fields and optional abundance variations. The model complexity also makes it more difficult to define the reference solution (the “true” parameter values), because emission often originates in some model sub-volume. The reference solutions were more likely to be more accurate in the variable-abundance case, when  $n_{\text{ref}} = \langle n(\text{H}_2) \rangle$  and  $N_{\text{ref}} = \langle N(\text{H}_2) \rangle$  were weighted not only by the beam but also by the density-dependent abundances, thus eliminating the low-density gas from these averages.

The EPF estimates of  $n_{\text{est}}$  and  $N_{\text{est}}$  were for individual transitions again mainly limited to narrow bands. Therefore, we calculated only distances between the reference value  $r_{\text{ref}}$  and the

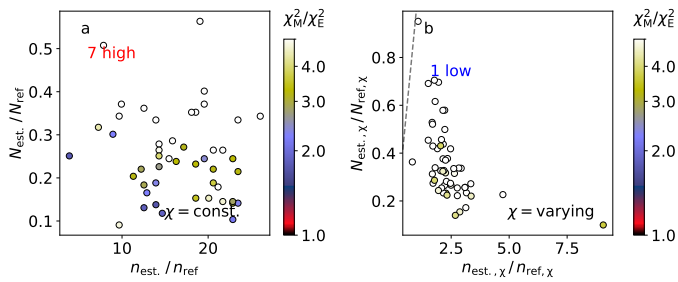


**Fig. 22.** As Fig. 21 but using estimates from the global  $\chi^2$  minimum instead of the closest position  $r_{\text{est}}$  along the  $\chi^2$  valley.

closest EPF solution point  $r_{\text{est}}$  with  $\chi^2$  values similar to the closest position along the  $\chi^2$  valley. The discrepancy between the two parameter positions typically showed a factor of two scatter, the density and column density being both either overestimated or underestimated. This results from the actual anticorrelation between  $n(\text{H}_2)$  and column density. One could of course reach the  $\chi^2$  valley also by moving along just one parameter axis, assuming no error in one parameter and larger error in the other. The selected shortest distance results in the discrepancy being attributed roughly equally between  $n(\text{H}_2)$  and  $N(\text{H}_2)$  (on logarithmic scale).

In several examples the constant- $\chi$  EPF estimates were unbiased or even on average larger than the reference values. In the variable- $\chi$  case the predictions were mostly lower, especially for the column density. The systematic errors could be even more than a factor of two, and individual clumps showed additionally more than a factor of two scatter in the  $N_{\text{est}}/N_{\text{ref}}$  ratio around the biased mean. The mean error and the scatter of the predicted density were smaller. Overall, the model errors often cause a discrepancy between the EPF estimates and the reference values that is more than a factor of two.

The above discrepancy (e.g.  $N_{\text{est}}$  vs.  $N_{\text{ref}}$ ) is only a lower limit for the formal error, since the global  $\chi^2$  minimum could be located even much further. Figure 22 is similar to Fig. 21 but uses the  $\chi^2$  minimum instead of  $r_{\text{est}}$  to characterise the errors in the EPF analysis of  $^{13}\text{CO}$  spectra. The bias in the column density values has grown to about a factor of three, and in the variable- $\chi$  case the density is now overestimated by a factor of  $\sim 2.5$ .

The model errors are thus an important source of uncertainty in the EPF analysis. They can be larger than the uncertainty of typical observational errors, which previous studies have shown to be typically of the order of a factor of two, of course depending on the used lines and the signal-to-noise ratios (Roueff et al. 2024).

Figure 23 shows an example of the effect of observational noise in the analysis of  $^{13}\text{CO}$  spectra from one of the MHD clumps. The frames show  $\chi^2$  for five  $T_{\text{kin}}$  values around the estimated  $\langle T(\text{kin}) \rangle$ . The  $\chi^2$  values are averages over the first three transitions, assuming 20% error estimates for the line intensities. In this case  $N_{\text{EPF}}$  is underestimated by  $\sim 0.3$  dex, and the best match with the expected density values is reached for 20% higher  $T_{\text{kin}}$ . However,  $T_{\text{kin}}$  is not well constrained, because the minimum  $\chi^2$  decreases towards higher  $T_{\text{kin}}$ , where density becomes underestimated. The white dots correspond to the  $\chi^2$  minima for 50 realisations of line intensities according with the assumed 20% observational noise. The points are distributed over the  $\chi^2$  minimum of the noiseless observations. In this case the model errors cause bias (shift relative to the expected parameter values, including the  $T_{\text{kin}}$  dependence) that is of the same order

of magnitude as the scatter caused by the statistical observational errors. If the observational errors were smaller, the errors would thus be dominated by the model errors.

### 5.3. Comparison of EPF and full radiative transfer modelling

EPF analysis could be replaced with full non-LTE radiative transfer modelling. This would result in significant increase in computational cost, but could be justified if the results were more accurate.

We examine briefly the example of a  $M=2M_{\odot}$ ,  $T_{\text{kin}}=15\text{ K}$  BE model, using the first three transitions of CS and  $\text{C}^{34}\text{S}$ . Figure 24a shows the general 3D shape of the  $\chi^2$  surface in the EPF fits. We made corresponding calculations with the LOC program, using a grid of cloud models that resulted from direct scaling of the correct cloud model to other densities, column densities, and temperatures. Since this grid includes the model that produced the synthetic observations, the minimum  $\chi^2$  value is in this case zero. The overall  $\chi^2$  distribution (Fig. 24b) is observed to be only roughly similar to that of the PEP calculations. In the EPF calculations the minimum  $\chi^2$  is however found at very low temperature (below 7 K), where the column density is underestimated by 40% and the volume density by a factor of four. If the temperature is fixed to the correct value ( $T_{\text{kin}}=15\text{ K}$ ), the column density is still underestimated by a factor of two, while the density is now overestimated by less than 40% (Fig. 24c-d). Overall, in LOC results the  $\chi^2$  minimum is better localised and, being based on the correct cloud model, is also unbiased (Fig. 24d).

In the case of real observations, cloud modelling of course has to be done with more limited knowledge of the real source structure. The use of a more realistic density profile (instead of the EPF single-point estimates) should result in some improvements, although it will be difficult to predict how this is reflected in the  $n(\text{H}_2)$  and column density accuracy. We made one test using the observations of the above BE model ( $M=2M_{\odot}$ ,  $T_{\text{kin}}=15\text{ K}$ ). We calculated a grid of RT models where the radial density distributions were Gaussian instead of the correct BE profiles. The  $\chi^2$  minimum of the Gaussian models was found at 12.7 K, with column density 30% and volume density just a couple of per cent above the correct value. Although the values are not exactly correct, this is still a significant improvement over the previous EPF results. If  $T_{\text{kin}}$  is fixed to 15 K, the relative improvement over EPF is smaller but still significant, with the full radiative transfer model overestimating the column density by 25% and underestimating  $n(\text{H}_2)$  by 10%.

This is only an isolated example based on the comparison of the  $\chi^2$  minima, without considering the full  $\chi^2$  surfaces. Furthermore, in a non-uniform cloud the correct values of  $n(\text{H}_2)$  and the column density are still subject to some interpretation. In the above test the Gaussian density profiles were rather similar to the actual BE profiles. If the approximation of the cloud structure were less accurate, also the improvement over the simpler EPF analysis would be more limited.

Full 3D RT calculations are still needed, if one wishes to match the observed line shapes (regarding the kinematics and the optical-depth effects), examine abundance variations (e.g. in connection with chemical models), combine observations that are clearly probing different parts of the object, or generally whenever deviations from homogeneity become evident in the observed data. Synthetic observations based on specific cloud models or simulations should of course also be preferentially based on full non-LTE RT calculations.

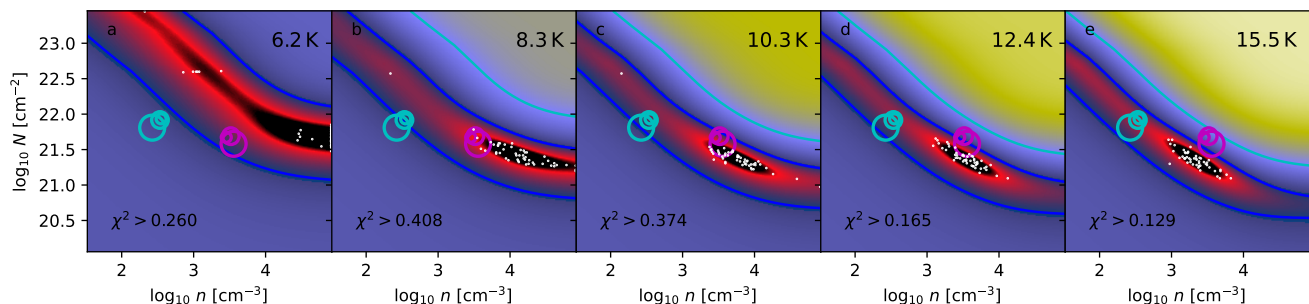


**Fig. 23.** EPF analysis of the first three  $^{13}\text{CO}$  transitions observed from an MHD clump. Results are shown for five  $T_{\text{kin}}$  values around the reference value  $T_{\text{ref}}$ . The images show the  $\chi^2$  planes for noiseless observations but assuming 20% error estimates. The contours are drawn at  $\chi^2=1$  (blue contour) and  $\chi^2=2$  (cyan contour). The minimum  $\chi^2$  values (average over the three transitions) are quoted in the frames. The white dots correspond to the  $\chi^2$  minima for 50 noise realisations consistent with the 20% observational noise.

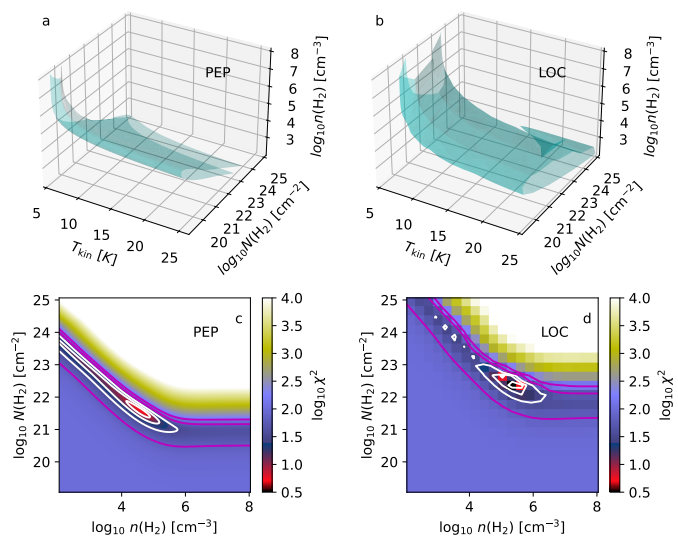


**Fig. 24.** Examples of  $\chi^2$  distributions in PEP and LOC analysis CS and  $\text{C}^{34}\text{S}$  spectra of a BE model with  $M=2M_{\odot}$  and  $T_{\text{kin}}=15\text{ K}$ . The upper frames show the general shape of the  $\chi^2 = 24$  surfaces. The lower frames show cross sections at the correct temperature of  $T_{\text{kin}} = 15\text{ K}$ . The white contours are drawn at  $\chi^2=7, 16, 32$  and the magenta contours at  $\chi^2=64$  and  $128$ , where the  $\chi^2$  values are the direct average over the included transitions ( $J = 1 - 0, 2 - 1, \text{ and } 3 - 2$  for CS and  $\text{C}^{34}\text{S}$ ).

#### 5.4. Implementation of the PEP program

In the test cases (Sect. 3), PEP reproduced accurately the results calculated with the RADEX program (van der Tak et al. 2007). In single-precision calculations differences appeared only for levels with populations  $\sim 10^{-8}$ , which are not likely to be important in real observations. This should enable faster calculations on GPUs. Calculations for  $\sim 10^5$  density and column density combinations could be computed with in about one second. This makes it possible to do the calculation on-the-fly, as diagnostic plots are made. However, for grids of moderate size (e.g.  $100 \times 100$  grid points), the run times were similar on both CPUs and GPUs (Appendix B). Therefore, there is generally no need to use a GPU, although that may still provide some speed-up in larger parameter studies (Fig. B.1).

In PEP the parallelisation is done over the density and column density values, using collisional coefficients precomputed for the chosen  $T_{\text{kin}}$ . Three-dimensional grids ( $n, N, T_{\text{kin}}$ ) are still

processed efficiently with a simple loop over temperature, especially since the  $T_{\text{kin}}$  grids tend to require fewer points. Full coverage of the relevant 3D parameter space (possibly combined with some priors) also makes it possible to quantify the formal uncertainties. Since the problem involves at most three parameters, this is faster than the use of for example MCMC methods. On the other hand, as shown in this paper, the model errors can be a significant or even the dominant source of uncertainty. Their effect is not captured by the  $\chi^2$  values.

There already exist several RADEX Python wrappers and re-implementations that make it easy to run EPF analysis for parameter grids. These include for example SpectralRadex (Holdship et al. 2021)<sup>2</sup> and pythonradex<sup>3</sup>. Although PEP can be significantly faster in large parameter studies, for small parameter grids the numerical efficiency is far less important.

The examples in this paper were all concerned with pure rotational spectra. In the case of a HFS structure lines, the photon escape probability should be higher because the optical depth is spread over a larger frequency range. The normal assumptions of EPF calculations may also not be valid for HFS spectra. In real clouds the photons that are emitted in one hyperfine transition can be reabsorbed only by transitions that are very close in frequency. This is in contradiction especially to the LVG model. We discuss in Appendix A one way of handling hyperfine transitions, so that the radiative connection is limited to a smaller velocity range. The comparison to full radiative transfer calculations shows that the main effects of HFS can thus be taken into account. However, EPF is always a strong simplification of the full radiative transfer problem. For example, hyperfine anomalies clearly require more complete radiative transfer modelling that can account for spatial excitation variations (e.g. Gonzalez-Alfonso & Cernicharo 1993).

## 6. Conclusions

We have presented PEP, a new computer program for the parallel calculation of line intensities based on the escape probability formalism (EPF). The comparison to other programs and the analysis of synthetic observations of spherically symmetric model clouds and clumps extracted from a MHD simulation have led to the following conclusions.

<sup>2</sup> <https://spectralradex.readthedocs.io>

<sup>3</sup> <http://pythonradex.readthedocs.io>

- The PEP program is found to be robust, with results that are in good agreement with predictions from other EPF programs.
- The parallelisation and the batch mode of calculating many parameter combinations in a single run makes the calculations efficient. In our tests the calculations with  $100 \times 100$  density and column density values took about one second.
- In the tested cases, single-precision floating point arithmetic provided sufficient accuracy. This can lead to some speed gains in GPU calculations.
- The full coverage of parameter grids provides useful information on the uncertainties and especially on the parameter degeneracies. However, the other major source of uncertainty, the model errors, can be probed only by examining full radiative transfer calculations of alternative models.
- For synthetic observations of spherical cloud models, the EPF predictions were often inconsistent with the expected density and column density values. The discrepancy can be more than a factor of two, even without any observational errors.
- The kinetic temperature is often poorly constrained, and even a small error in  $T_{\text{kin}}$  can be associated with a large shift (up to a factor of several) in the predicted  $n(\text{H}_2)$  and column density values. This is true especially when lines are close to saturation due to high optical depths.
- The analysis of MHD clumps showed the EPF estimates to be usually correct to within a factor of two (models with variable abundances and correct  $T_{\text{kin}}$ ). Different molecules showed varying amounts of systematic errors. There were a few outliers with order-of-magnitude errors, and not limited to just optically very thick lines.
- The overall shape of the  $\chi^2$  surfaces can be similar in EPF and full RT calculations. However, especially when the RT model approximates the source structure well, the full RT calculations will provide more accurate parameter estimates. RT modelling is also needed in studies of the line profiles or whenever deviations from source homogeneity are clear.
- We discussed approximate handling of hyperfine structure lines in EPF calculations. The results were qualitatively similar to those seen in full non-local radiative transfer calculations. However, EPF is clearly not suitable, for example, for the modelling hyperfine anomalies.

Ebert, R. 1955, *Zeitschrift für Astrophysik*, 37, 217  
 Goldreich, P. & Scoville, N. 1976, *ApJ*, 205, 144  
 Goldsmith, P. F. 2001, *ApJ*, 557, 736  
 Gonzalez-Alfonso, E. & Cernicharo, J. 1993, *A&A*, 279, 506  
 Harries, T. J., Haworth, T. J., Acreman, D., Ali, A., & Douglas, T. 2019, *Astronomy and Computing*, 27, 63  
 Hogerheijde, M. R. & van der Tak, F. F. S. 2000, *A&A*, 362, 697  
 Holdship, J., Viti, S., Martín, S., et al. 2021, *A&A*, 654, A55  
 Juvela, M. 1997, *A&A*, 322, 943  
 Juvela, M. 2020, *A&A*, 644, A151  
 Juvela, M., Mannfors, E., Liu, T., & Tóth, L. V. 2022, *A&A*, 666, A74  
 Juvela, M., Padoan, P., & Jimenez, R. 2003, *ApJ*, 591, 258  
 Juvela, M. & Ysard, N. 2011, *ApJ*, 739, 63  
 Navarro-Almaida, D., Le Gal, R., Fuente, A., et al. 2020, *A&A*, 637, A39  
 Neufeld, D. A. & Kaufman, M. J. 1993, *ApJ*, 418, 263  
 Neufeld, D. A., Lepp, S., & Melnick, G. J. 1995, *ApJS*, 100, 132  
 Padoan, P., Juvela, M., Pan, L., Haugbølle, T., & Nordlund, Å. 2016, *ApJ*, 826, 140  
 Peters, T., Banerjee, R., Klessen, R. S., & Mac Low, M.-M. 2011, *ApJ*, 729, 72  
 Roueff, A., Pety, J., Gerin, M., et al. 2024, *A&A*, 686, A255  
 Rybicki, G. B. & Hummer, D. G. 1992, *A&A*, 262, 209  
 Schöier, F. L., van der Tak, F. F. S., van Dishoeck, E. F., & Black, J. H. 2005, *A&A*, 432, 369  
 Shirley, Y. L. 2015, *PASP*, 127, 299  
 Sobolev, V. V. 1960, *Moving Envelopes of Stars*  
 Tomida, K., Tomisaka, K., Matsumoto, T., et al. 2013, *ApJ*, 763, 6  
 Tunnard, R. & Greve, T. R. 2016, *ApJ*, 819, 161  
 Tunnard, R., Greve, T. R., Garcia-Burillo, S., et al. 2015, *ApJ*, 815, 114  
 van der Tak, F. F. S., Black, J. H., Schöier, F. L., Jansen, D. J., & van Dishoeck, E. F. 2007, *A&A*, 468, 627  
 van Zadelhoff, G. J., Dullemond, C. P., van der Tak, F. F. S., et al. 2002, *A&A*, 395, 373

Overall, the model errors can be as important or even more important than the observational errors and should be taken into account when estimating the overall reliability of the EPF analysis. The accuracy of parameter estimates could also improve, if some of the parameters had fixed values or tight priors. These could be based on ancillary observations, such as direct  $T_{\text{kin}}$  measurements with other species or even rough  $N(\text{H}_2)$  estimates from independent dust observations.

*Acknowledgements.* MJ acknowledges the support of the Research Council of Finland Grant No. 348342.

## References

Asensio Ramos, A. & Elitzur, M. 2018, *A&A*, 616, A131  
 Bernes, C. 1979, *A&A*, 73, 67  
 Bonnor, W. B. 1956, *MNRAS*, 116, 351  
 Bron, E., Daudon, C., Pety, J., et al. 2018, *A&A*, 610, A12  
 Cannon, C. J. 1973, *ApJ*, 185, 621  
 Commerçon, B., Hennebelle, P., Audit, E., Chabrier, G., & Teyssier, R. 2010, *A&A*, 510, L3  
 de Jong, T., Chu, S., & Dalgarno, A. 1975, *ApJ*, 199, 69  
 Dullemond, C. P. & Turolla, R. 2000, *A&A*, 360, 1187

## Appendix A: Hyperfine structure lines

In the normal EPF method the photon escape probabilities are calculated for isolated Gaussian line profiles. However, many molecules exhibit hyperfine structure (HFS), where the interaction of molecular rotation with an atomic nucleus of non-zero spin results in the splitting of the energy levels. Typical astronomical observations of HFS spectra include the low rotational transitions of  $\text{N}_2\text{H}^+$ , HCN, HNC, and  $\text{C}^{17}\text{O}$ , as well as the inversion transitions of ammonia, especially  $\text{NH}_3(1,1)$  and  $\text{NH}_3(2,2)$ . When spectral lines are split to a number of components along the frequency axis, the individual HFS components have lower optical depths, and this results in an overall increase in the photon escape probability  $\beta$ . Since  $\beta$  is a non-linear function of  $\tau$ , it scales differently for HFS components of different intensity, even before the additional complication of potential frequency overlap between HFS components is taken into account. The spectral overlap depends on the assumed velocity field and the line width  $FWHM$ . HFS is therefore not a simple rescaling of the normal  $\beta$  values and must be estimated separately for each species and values of the optical depth and line  $FWHM$ .

The normal EPF criteria may not be meaningful in the case of HFS lines. Under the LVG assumption the emission from every hyperfine component could be absorbed by any other hyperfine component. In real clouds this is possible only between neighbouring components, typically over a frequency interval corresponding to some  $\sim 1 \text{ km s}^{-1}$  in velocity.

We tested one possible method to take into account the HFS effects, under the assumption that the relative level populations of the HFS components are in LTE. The  $\beta$  values are first calculated in the normal fashion for Gaussian lines (i.e. according to either the LVG, slab, or homogeneous-sphere model). For the HFS transitions these are rescaled with correction factors  $\xi(\tau) = \beta(\text{HFS})/\beta(\text{Gaussian})$ . Here  $\beta(\text{Gaussian})$  is the normal escape probability for isolated Gaussian line profiles. To calculate  $\xi$ , we assume a static medium with the prescribed line  $FWHM$ , and compute the correction  $\xi(\tau)$  for a single line of sight, as a function of the total optical depth.

The escape probability for a Gaussian line in a static medium is

$$\beta(\text{Gaussian}) = \frac{\int \phi(v) e^{-\tau\phi(v)} dv}{\int \phi(v) dv}, \quad (\text{A.1})$$

where  $\phi_v$  is the profile function with  $\int \phi_v dv = 1$ . For  $N_C$  HFS components with velocity offsets  $\Delta v_i$ , the corresponding expression for an HFS line is

$$\beta(\text{HFS}) = \frac{\int \sum_i^{N_C} I_i \phi(v + \Delta v_i) e^{-\tau \sum_i^{N_C} I_i \phi(v + \Delta v_i)} dv}{\int \sum_i^{N_C} I_i \phi(v + \Delta v_i) dv}. \quad (\text{A.2})$$

The optical depth  $\tau^\Sigma$  is the sum over the components,

$$\tau_v^\Sigma = \tau \sum_i^{N_C} I_i \phi(v + \Delta v_i), \quad (\text{A.3})$$

where  $\tau$  is the total line optical depth. Here  $I_i$  are the relative weights of the HFS components with  $\sum_i I_i = 1$ . Thus the denominator of Eq. (A.2) is again equal to one.

In the absence of specific information on the source velocity field, the proposed method is only one possible way to estimate the actual  $\beta$  values in a source. However, it captures the expected increase for  $\beta$  of the HFS transition and is an improvement over simply ignoring the HFS structure.

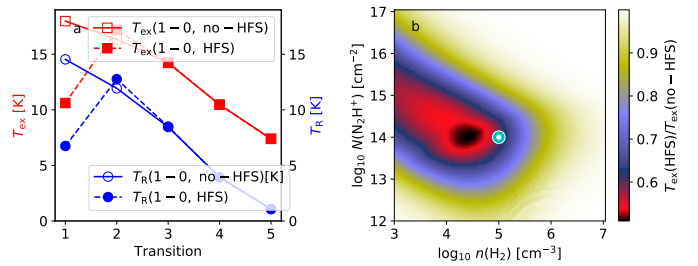


**Fig. A.1.** Comparison of EPF results for  $\text{N}_2\text{H}^+$  when the HFS of the  $J = 1 - 0$  line is taken into account (Sect. A) or is ignored. Frame a shows the  $T_{\text{ex}}$  and  $T_{\text{R}}$  values for  $T_{\text{kin}} = 20 \text{ K}$ , with  $n(\text{H}_2) = 10^5 \text{ cm}^{-3}$  and  $N(\text{N}_2\text{H}^+) = 10^{14} \text{ cm}^{-2}$  (cyan circle in frame b). The assumed line width is  $FWHM = 1 \text{ km s}^{-1}$ . Frame b shows the ratio of  $T_{\text{ex}}(1-0)$  values when the HFS is taken into account and when it is ignored.

Figure A.1 compares PEP calculations where the hyperfine structure of the  $J = 1 - 0$  line of  $\text{N}_2\text{H}^+$  is either ignored or taken into account. The inclusion of the hyperfine structure naturally increases the photon escape probability and leads to significant decrease in the excitation temperature of the  $J = 1 - 0$  transition. The difference is reflected in the  $J = 2 - 1$  transition, while the next levels remain practically unchanged. Figure A.1b shows the ratio of the predicted  $T_{\text{ex}}(1-0)$  values over a wide range of  $n(\text{H}_2)$  and  $N(\text{H}_2)$ . The effect has a maximum of close to a factor of two, but it disappears at high densities due to thermalisation.

For comparison with the above approximation, we performed one calculations with LOC, using a homogeneous spherical model with a temperature of  $T_{\text{kin}}=20 \text{ K}$ . While PEP provides a single set of level populations and thus a single value of  $T_{\text{ex}}$ , in LOC results the excitation varies radially. Therefore the results of the two programs are not expected to be identical even without the HFS structure. To characterise the LOC models we used the mean column density over the projected model area and the mean value of  $T_{\text{ex}}$  over the model volume.

Figures A.1 and A.2 show that the effect of the hyperfine structure, and the location and general shape of the parameter region where the inclusion of hyperfine structure causes a large drop in  $T_{\text{ex}}$  are similar. However, the  $T_{\text{ex}}(\text{HFS})/T_{\text{ex}}(\text{no-HFS})$  minimum is in PEP calculations at a higher density and lower column density.

## Appendix B: PEP run times

To characterise the PEP performance in terms of run times, we ran a series of tests using the CO molecule, with  $T_{\text{kin}} = 15 \text{ K}$  and including the first 20 rotational levels. PEP was run for different sizes of the  $(n, N)$  grid, which however always covered the same total range of parameter values. The iterations were stopped when the change in level populations per iteration was less than  $10^{-5}$  relative or less than  $10^{-10}$  in absolute terms. The latter ensures that levels with insignificant population do not prevent the iterations from stopping.

The run times are shown in Fig. B.1a. For most practical applications (i.e. with up to a few times  $10^4$  parameter combinations per run), the run time is roughly constant and less than one second. Thus, the cost is dominated by the initialisations done in the host Python program. Thereafter the run times approach the expected linear dependence on the number of parameter combinations. In the test system, GPU becomes faster than CPU only when the number of parameter combinations is above a few times  $10^4$ . The GPU results in Fig. B.1 are shown for a mod-

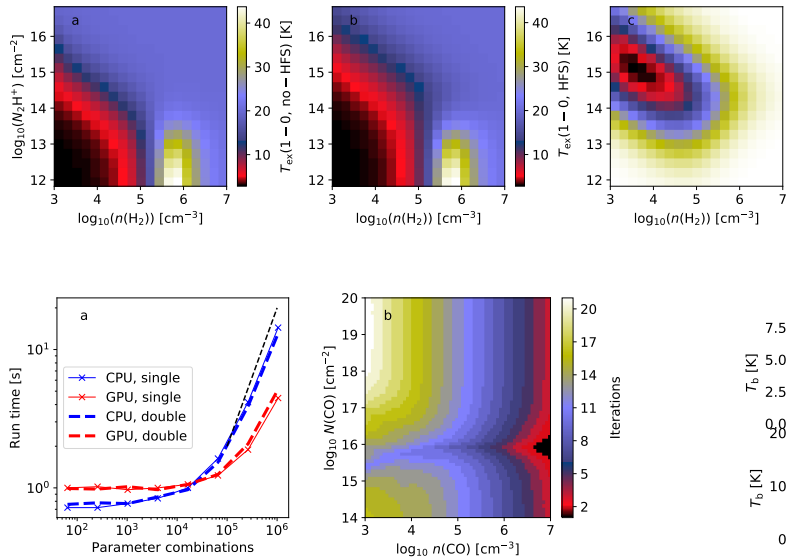


**Fig. B.1.** Examples of PEP run times. Frame a shows the run time on CPU (blue curve) and GPU (red curve) as a function of the number of parameter combinations ( $n, N$ ) for  $T_{\text{kin}} = 15$  K. The calculations included the first 20 rotational levels of the CO molecule. The black dashed line indicates the slope of a one-to-one relation. Frame b shows how the number of iterations needed to reach the selected convergence criteria.

ern laptop, using an external desktop GPU. Unexpectedly, there was no significant difference in calculations performed in single precision and double precision. Because the main computational cost in the solving of the statistical equilibrium equations and that scales with the third power of the number of excitation levels, the advantage of using GPUs (and single precision) should become significant in larger problems, although this was not yet observed in our tests.

Figure B.1b shows the parameter ranges and the number of iterations required by the PEP program. As noted in Sect. 2, the initial level populations are set in according to the LTE condition with  $T = T_{\text{kin}}$ . This also partially explains the low number of iterations needed at the highest densities, where the solution remains close to LTE. However, at high column densities and somewhat lower volume densities (optically thick but non-thermalised lines), it might be necessary to check further that the iterations have not ended prematurely, due to a slower convergence.

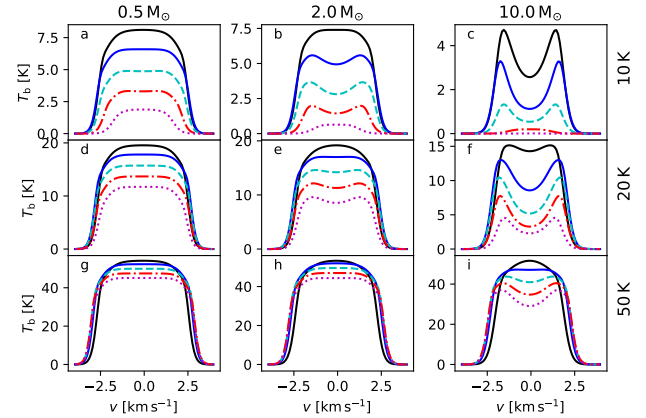
## Appendix C: Additional Bonnor-Ebert models

### C.1. Model spectra for Bonnor-Ebert spheres

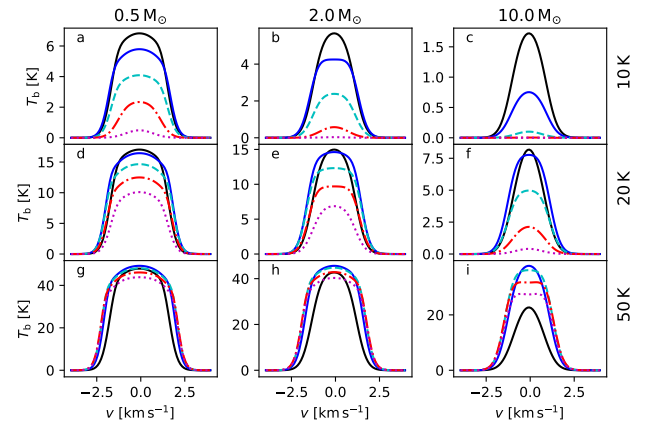
Figures C.1-C.5 show synthetic spectra for BE models that were used as inputs in the EPF analysis in Sect. 4.1. Each plot shows the spectra for three values of the model  $T_{\text{kin}}$  and mass, each frame including line profiles for the first five rotational transitions observed with the  $FWHM = R_0/3$  beam. Optically less thick species ( $\text{C}^{18}\text{O}$ ,  $\text{C}^{34}\text{S}$ , and  $\text{H}^{13}\text{CO}^+$ ) are not plotted as these have always nearly Gaussian profiles.

Figure C.6 shows the EPF analysis of an isothermal Bonnor-Ebert model separately for three  $^{12}\text{CO}$  and  $^{13}\text{CO}$  transitions. The figure is thus similar to Fig. 5 except for the use of different molecules and the more massive model cloud of  $M = 10 M_{\odot}$ .

**Fig. A.2.** Results from LOC runs with homogeneous spherical models and the  $\text{N}_2\text{H}^+$  molecule. Frames a and b show, respectively, the mean  $T_{\text{ex}}(1-0)$  values when the  $J = 1-0$  hyperfine structure is ignored or is taken into account. Frame c shows their ratio and is analogous to the PEP results in Fig. A.1. The axes are the mean values of the model cloud density  $n(\text{H}_2)$  and  $\text{N}_2\text{H}^+$  column density. The gas kinetic temperature is  $T_{\text{kin}} = 20$  K.



**Fig. C.1.** Synthetic  $^{12}\text{CO}$  spectra for 1D BE models.



**Fig. C.2.** Synthetic  $^{13}\text{CO}$  spectra for 1D BE models.

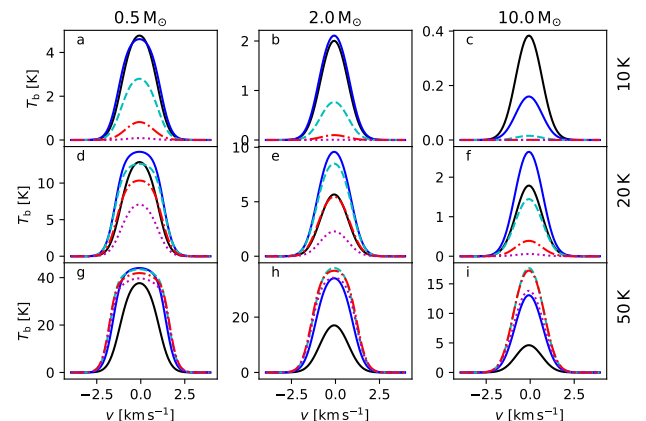


**Fig. C.3.** Synthetic  $^{13}\text{CO}$  spectra for 1D BE models.

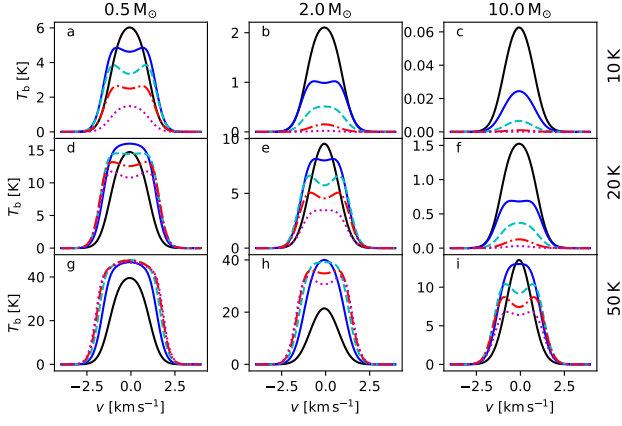


**Fig. C.4.** Synthetic CS spectra for 1D BE models.

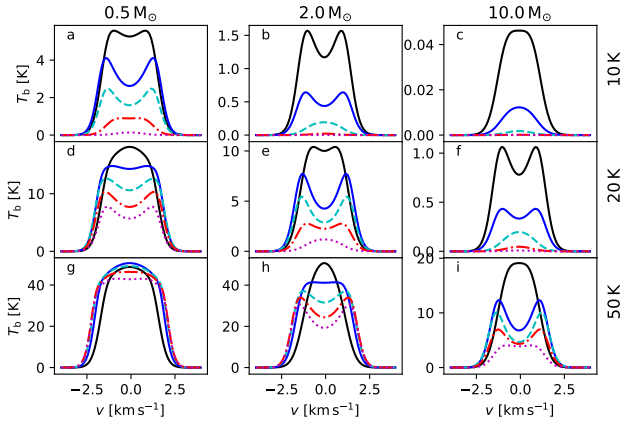


**Fig. C.5.** Synthetic HCO<sup>+</sup> spectra for 1D BE models.

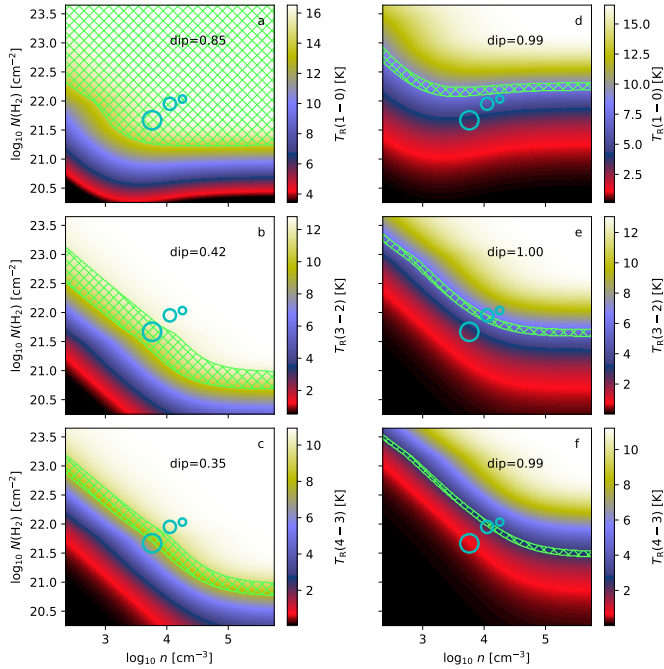


**Fig. C.6.** As Fig. 5 but for <sup>12</sup>CO (left frames) and <sup>13</sup>CO (right frames), for the cloud model with 10M<sub>⊙</sub> and  $T_{\text{kin}}=20$  K.

## C.2. Plots for isothermal Bonnor-Ebert models

Section 4.1.1 discussed the results for isothermal BE spheres. Figure 7 showed the discrepancy between the reference values and the EPF estimates for one of the cloud models. Figures C.7-C.10 show further examples for four models of different mass and temperature  $T_{\text{kin}}$ .

Figure C.11 shows  $\chi^2$  planes for <sup>13</sup>CO observations of the isothermal BE sphere with  $M=2M_{\odot}$  and  $T_{\text{kin}}=20$  K, for analysis performed at three different  $T_{\text{kin}}$  values. The figure is similar to Fig. 8 but for a model where results are more sensitive to the assumed value of  $T_{\text{kin}}$ .

Figure 12 showed EPF-predicted  $\chi^2$  values for one BE cloud model, for combined CS and C<sup>34</sup>S observations, with the C<sup>34</sup>S abundances that were either correct or had 50% error. Figure C.12 shows additional examples for the 2 M<sub>⊙</sub> cloud models with two values of  $T_{\text{kin}}$ .

## C.3. Non-isothermal Bonnor-Ebert models

Figures C.13 and C.14 show a comparison of EPF results for non-isothermal models and the combination of CS and C<sup>34</sup>S lines. The kinetic temperature is fixed to the correct value, but the analysis is also repeated with C<sup>34</sup>S abundances that are 50% lower or higher than the actual value. The figures differ only by the radial  $T_{\text{kin}}$  gradient being positive in Fig. C.13 and negative in Fig. C.14.

## Appendix D: Additional figures on MHD clumps

Section 4.2 showed results for clumps selected from the MHD simulation. The discrepancy between the reference values and EPF estimates based on <sup>12</sup>CO and <sup>13</sup>CO observations were shown in Figs. 20-21. Figures D.1-D.9 show further examples for other molecules and models with (ad hoc) higher density.

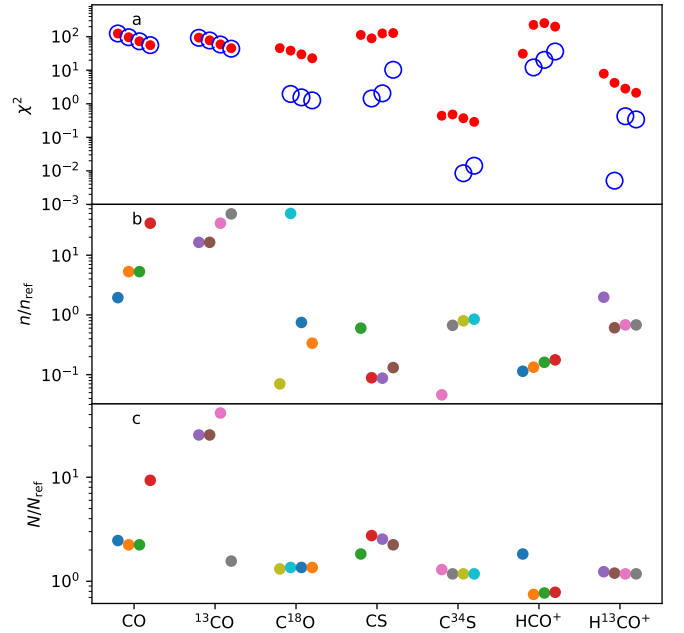


**Fig. C.7.** As Fig. 7 but for the  $M=0.5M_{\odot}$  model with  $T_{\text{kin}}=10$  K



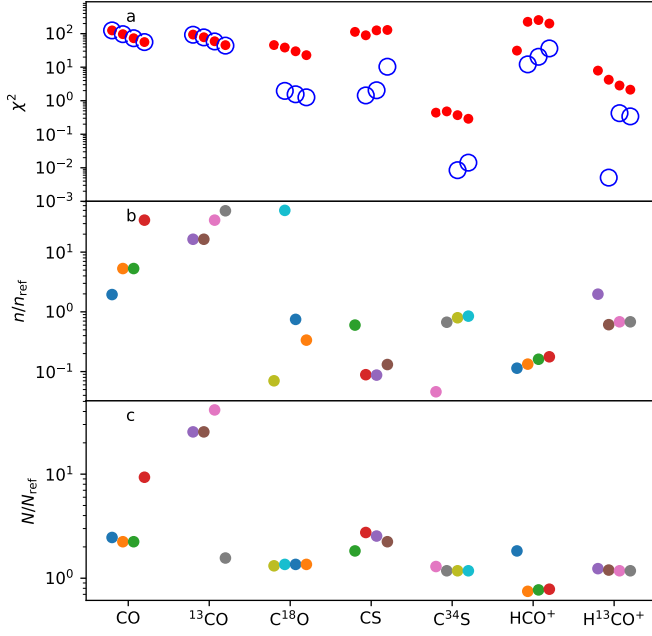


**Fig. C.8.** As Fig. 7 but for the  $M = 0.5M_{\odot}$  model with  $T_{\text{kin}}=50$  K

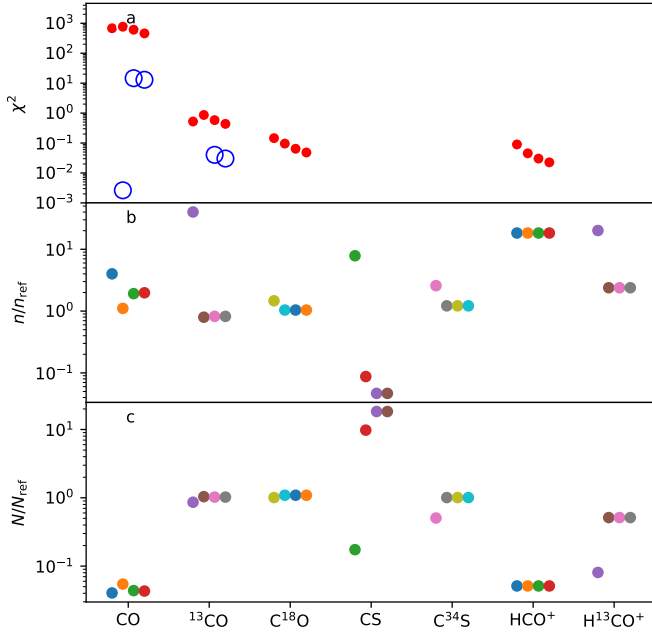


**Fig. C.9.** As Fig. 7 but for the  $M = 10M_{\odot}$  model with  $T_{\text{kin}}=10$  K

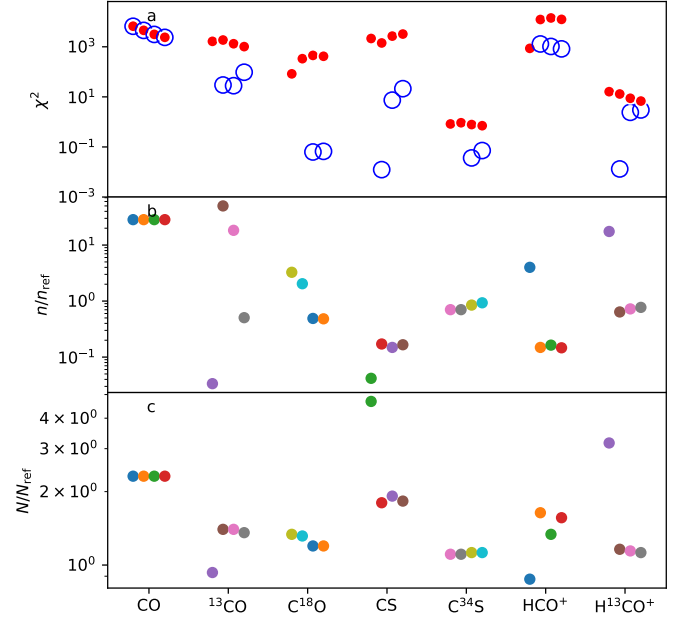


**Fig. C.10.** As Fig. 7 but for the  $M = 10M_{\odot}$  model with  $T_{\text{kin}}=50$  K

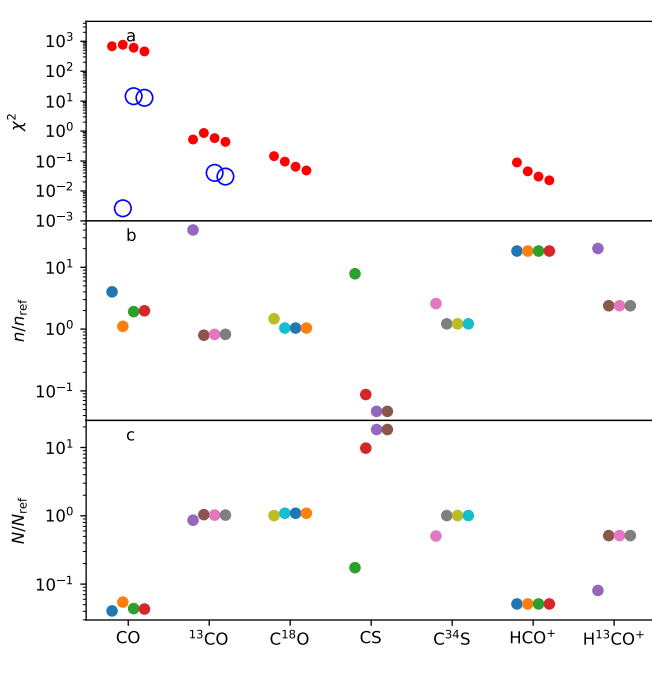


**Fig. C.11.** As Fig. 8 but for  $^{13}\text{CO}$  spectra of the isothermal BE model with  $M = 2M_{\odot}$  and  $T_{\text{kin}}=20$  K.

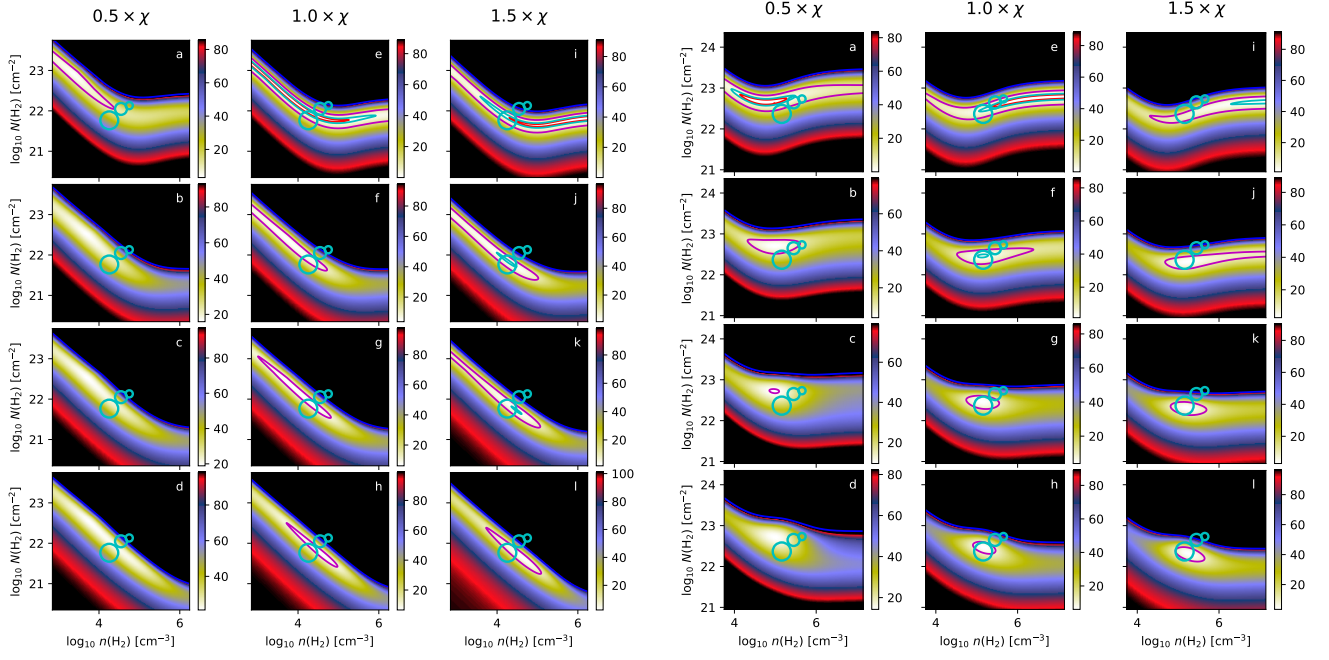


**Fig. C.12.** As Fig. 12 but for the  $2M_{\odot}$  cloud model with  $T_{\text{kin}}=10$  K (left frames) and  $T_{\text{kin}}=20$  K (right frames).

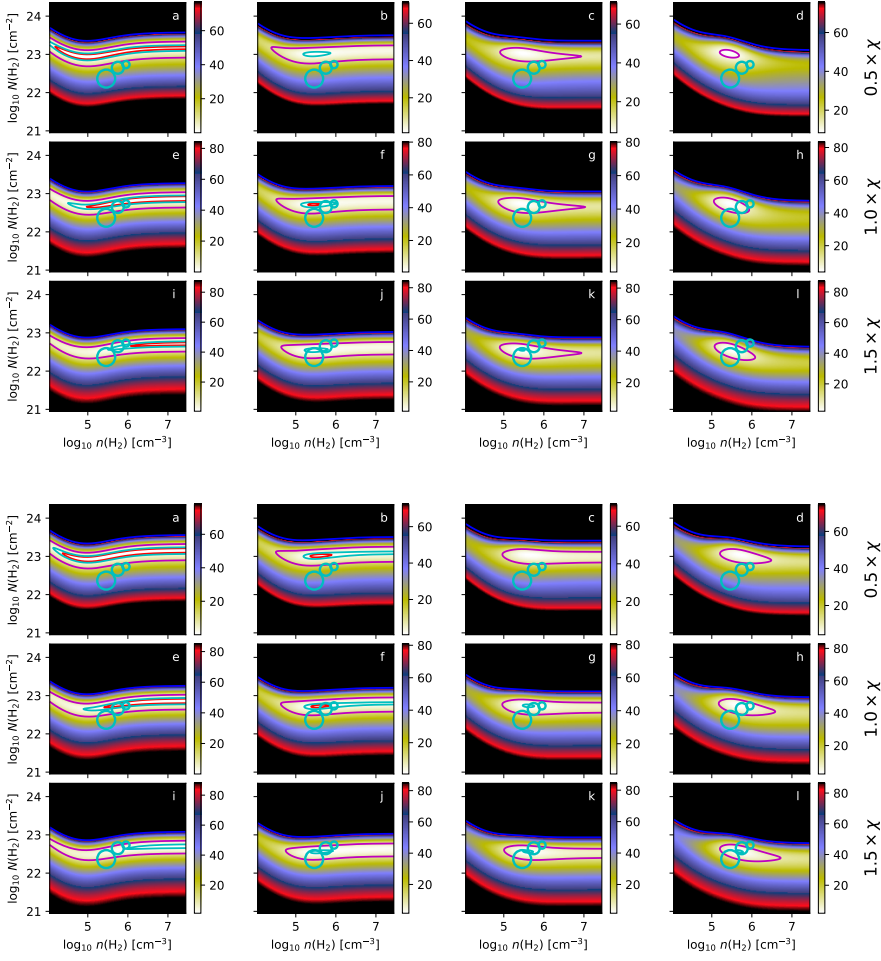


**Fig. C.13.** Results for BE models with  $M = 0.5 M_{\odot}$  and  $\langle T_{\text{kin}} \rangle = 10$  K, for  $T_{\text{kin}}$  increasing outwards. The frames from left to right correspond to the combination of 1-4 lowest rotation transitions of CS and  $\text{C}^{34}\text{S}$ . The rows correspond to three assumptions of the  $\text{C}^{34}\text{S}$  abundance (middle row with the correct value). Contours are drawn at  $\chi^2=1, 2, 10$ , and  $100$  (red, cyan, magenta, and blue colours, respectively). The cyan circles indicate the reference values for the central line of sight (smallest circle), for the  $\text{FWHM} = R_0/3$  beam (as used for the input synthetic observations), and for the  $\text{FWHM} = R_0$  beam (largest circle).

**Fig. C.14.** As Fig. C.13 but with  $T_{\text{kin}}$  decreasing outwards in the model cloud.

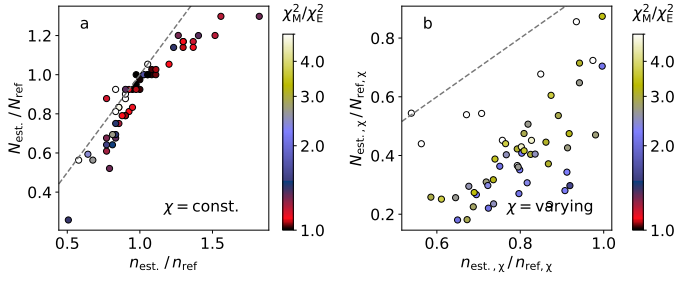


**Fig. D.1.** As Fig. 20 but for models with five times higher volume density.

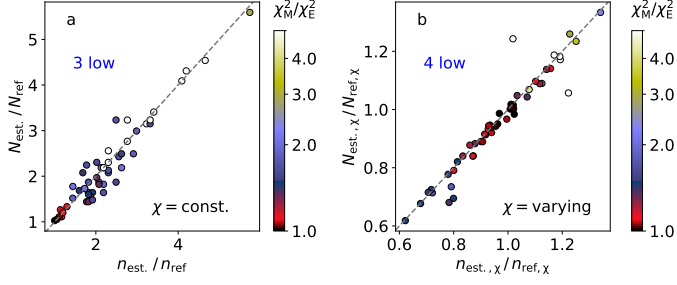


**Fig. D.2.** As Fig. 20 but for the HCO<sup>+</sup> molecule.

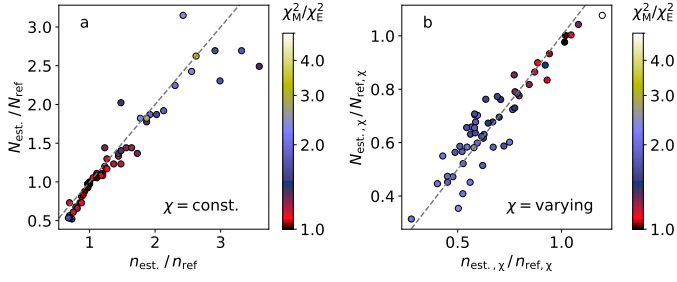


**Fig. D.3.** HCO<sup>+</sup> results similar to Fig. D.2 but for models with five times higher volume density.

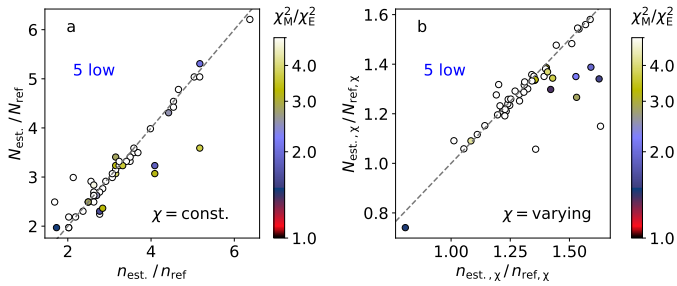


**Fig. D.4.** As Fig. 20 but for the H<sup>13</sup>CO<sup>+</sup> molecule.

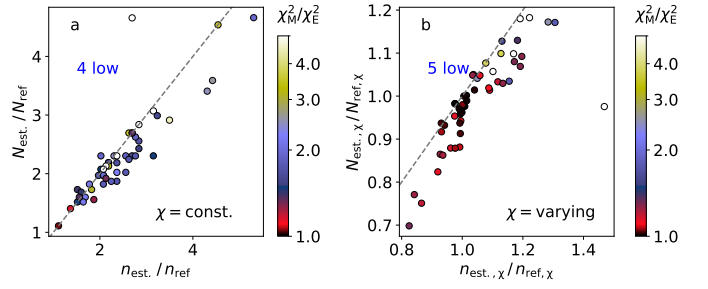


**Fig. D.5.** H<sup>13</sup>CO<sup>+</sup> results, as Fig. D.4 but for models with five times higher density.

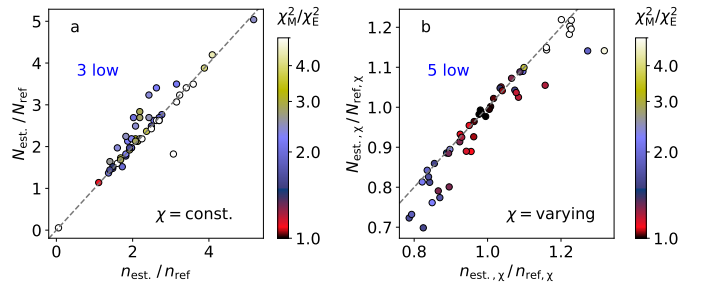


**Fig. D.6.** As Fig. 20 but for the CS molecule.

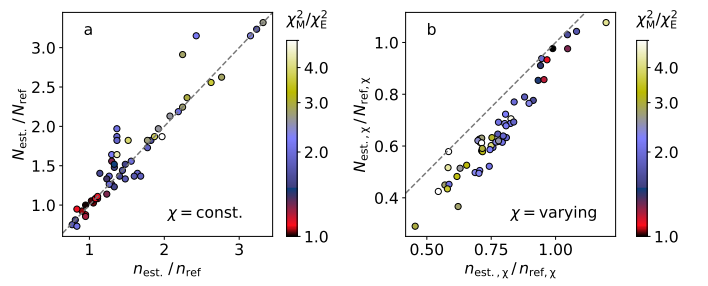


**Fig. D.7.** CS results similar to Fig. D.6 but for models with five times higher volume density.

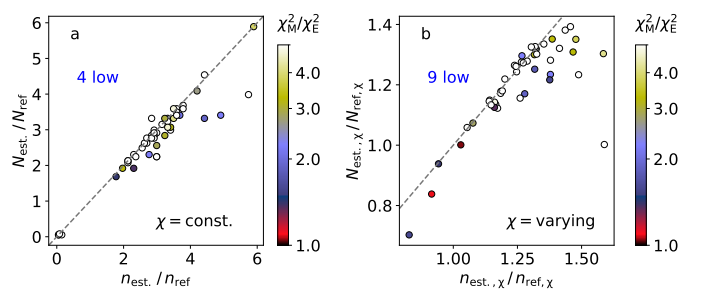


**Fig. D.8.** As Fig. 20 but for the C<sup>34</sup>S molecule.

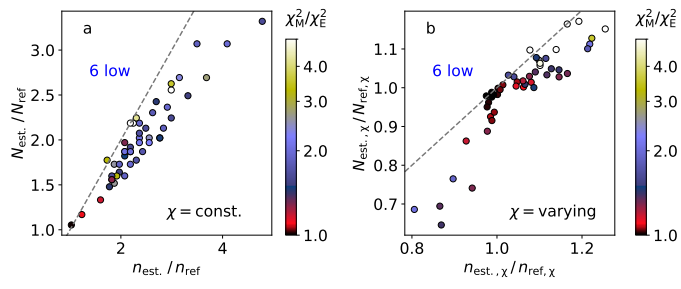


**Fig. D.9.**  $C^{34}$ S results similar to Fig. D.8 but for models with five times higher volume density.